# CO6-1

## SAXS/SANS Analysis of *Pinctada fucata* Shell Matrix Protein Nacrein

Y. Namikawa[1], K. Morishima[2], R. Inoue[2], M. Sugiyama[2], and M. Suzuki[1]

[1] Graduate School of Agricultural and Life Sciences, The University of Tokyo
[2] Institute for Integrated Radiation and Nuclear Science, Kyoto University

**INTRODUCTION:** Organisms utilize proteins containing intrinsically disordered regions (IDRs) to express specific functions, and understanding their dynamics is essential for elucidating biological phenomena. Small-angle X-ray scattering (SAXS) and small-angle neutron scattering (SANS) directly analyze molecular size and shape in solution, useful for analysis of IDR-containing proteins. This study focuses on nacrein, a shell matrix protein of the pearl oyster (*Pinctada fucata*), which is a model organism for biomineralization. Nacrein interacts with calcium carbonate ($CaCO_3$), inhibiting random $CaCO_3$ crystal precipitation and promoting high-purity $CaCO_3$ deposition. Nacrein is a multi-domain protein consisting of a structured carbonic anhydrase domain and a GXN domain (an IDR with Gly-Xaa-Asn repeats). To understand nacrein's role in shell formation, elucidating the structural characteristics of the GXN domain is essential. Therefore, this study aims to obtain structural information of nacrein in solution through SAXS and SANS measurements.

**EXPERIMENTS:** Nacrein was extracted and purified from natural pearl oyster shells. Before SAXS measurements, nacrein was purified by size-exclusion chromatography (SEC) to obtain a 1.24 mg/mL sample. Additionally, a solution containing 1.22 mg/mL nacrein and 14 mM $CaCO_3$ was prepared. SAXS measurements were performed using the Cu-source small-angle X-ray scattering instrument (NANOPIX), installed at KURNS. For SANS, two nacrein samples with solvents of 0% $D_2O$ and 100% $D_2O$ were prepared via SEC, and measurements were conducted at D22 of the Institut Laue-Langevin (ILL).

**RESULTS:** The overall structure of nacrein in solution was evaluated by SAXS (Fig. 1). Kratky analysis showed typical scattering behavior for proteins containing both a structured domain and an IDR. Furthermore, the pair-distance distribution function $P(r)$ revealed a maximum intramolecular distance $D_{max}$ of 93 Å. This value is significantly larger than expected for the structured carbonic anhydrase domain, predicted from its amino acid composition, indicating a highly extended conformation of the GXN domain in solution. Upon analyzing structural changes during interaction with $CaCO_3$, no significant differences were observed in the SAXS profiles with or without $CaCO_3$, indicating that nacrein interacts with $CaCO_3$ without undergoing major conformational changes in its overall structure. Subsequent SANS measurements yielded different scattering profiles in 0% $D_2O$ and 100% $D_2O$ (Fig. 2). The radius of gyration $R_g$ obtained by Guinier analysis was 21.5 Å in 0% $D_2O$ and 26.1 Å in 100% $D_2O$. The difference in $R_g$ arises because the scattering length densities of Gly, Asn, and Asp, which primarily constitute the GXN domain, differ significantly between 0% $D_2O$ and 100% $D_2O$. Obtaining different spectra by varying the radiation source and solvent $D_2O$ ratio for the same protein has the potential to refine structural ensembles of IDRs obtained from MD simulations. In the future, we aim to yield plausible structural ensembles of nacrein by combining MD simulations with SAXS/SANS.

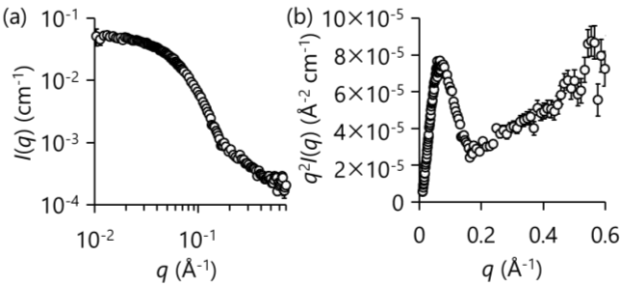


Fig. 1. (a) SAXS profile (b) Kratky plot.

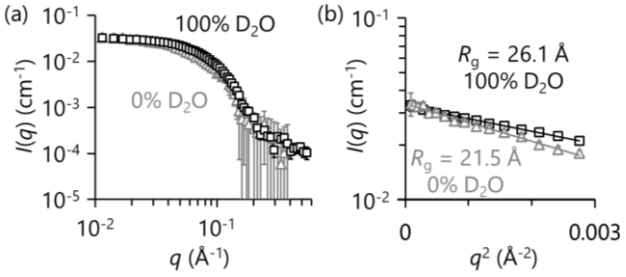


Fig. 2. (a) SANS profiles (b) Guinier plots.

# CO6-2

## Analysis of the Mint3–FIH-1 interaction that regulates hypoxic stress response.

M. Hoshino[1], K. Morishima [2], M. Shimizu [3], R. Inoue[4] and M. Sugiyama[2]

[1] *Graduate School of Pharmaceutical Sciences, Kyoto University*
[2] *Institute for Integrated Radiation and Nuclear Science, Kyoto University*

**INTRODUCTION:** Oxygen is essential for many organisms to produce ATP efficiently from nu-trients in food. Temporal or local drop of oxygen level induces cells to change the metabolic pathway, which is known as hypoxia stress responses. The responses are mainly triggered by hy-poxia inducible factors (HIFs) that activate transcription of a group of genes. Under the normal oxygen conditions, transcriptional activities of HIFs in the cells are inhibited by the factor inhibiting HIF-1 (FIH-1). On the other hand, several cells including tumor cells and macrophages, metabo-lize nutrients exclusively by nonoxidative glycolytic pathway even under the normal oxygen levels. Munc-18 inter-acting protein 3 (Mint3) is recently found to activate the hypoxia responses by bind-ing and inhibiting the activity of FIH-1 in these cells [1]. Although the N-terminal 214 residues (Mint3NT) are found to be necessary for the interaction with FIH-1 to inhibit its activity, little is known about inhibitory mechanisms.

**EXPERIMENTS:** High-expression systems for the N-terminal fragment proteins of Mint3 (Mint3NT) and smaller fragments (Mint3(1–117) and Mint3(101–214)), as well as full-length FIH-1 were constructed by E. coli BL21 strains. The proteins were expressed in bacteria grown in LB-broth and $^{15}$N-enriched M9 minimal medium to produce unlabeled and $^{15}$N-labeled proteins, respectively. NMR experiments were performed on a Bruker Avance 600 spectrometer equipped with a triple-resonance probe. A typical $^{1}$H-$^{15}$N HSQC experiments were performed at protein con-centration of 50 μM. The solvent used were 20 mM sodium phosphate (pH 7.3), and 10% $D_2O$.

**RESULTS:** We measured the $^{1}$H-$^{15}$N HSQC spectrum of Mint3NT, and found that the dis-persion of resonance peaks was very poor particularly along the 1H-axis, suggesting the absence of strong hydrogen-bonding interac-tions (Figure 1). Furthermore, the superposi-tion of two HSQC spectra separately recorded for the fragment proteins of Mint3NT (Mint3(1-117) and Mint3(101-214)) repro-duced the spectrum of whole protein (Mint3NT), suggesting the absence of signif-icant interaction between the N- and C-terminal regions of Mint3NT.

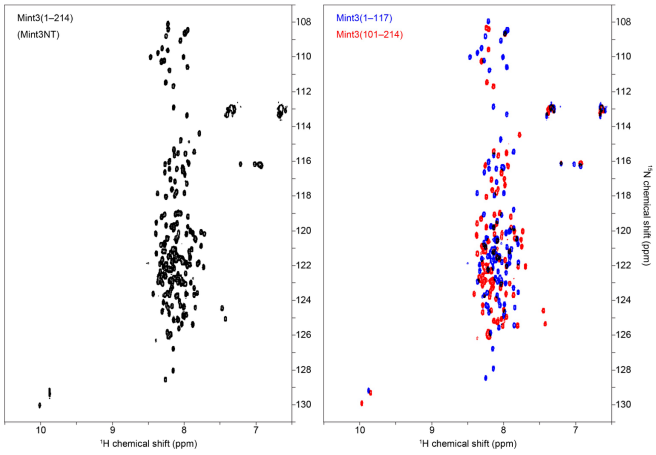


**Fig. 1** $^{1}$H-$^{15}$N HSQC spectra of Mint3(1–214) (left) and the superposition of fragment proteins (Mint3(1–117) and Mint3(101–214) (right).

We also performed a titration experiment of $^{15}$N-labled Mint3NT by unlabeled FIH-1, and found that the peak intensities for many residues were remarkably decreased in a concentration dependent manner. We analyzed several 3D-triple resonance experiments, and succeeded to unam-biguously assign more than 95% of residues. By mapping the change in the peak intensity along the primary structure of the protein, we found that a broad range of residues were significantly affected by the addition of unlabeled FIH-1, suggesting the involvement of these residues in the interaction between Mint3NT and FIH-1.

**REFERENCES:**

[1] K. Okano *et al.*, Nucl. Instr. and Meth., **186** (1981) 115-120.

# CO6-3

## Investigations of Ultra-High Dose Rate Electron Beam Using Alanine

S. Srisuwan[1], H. Tanaka[2], M. Nakayama[1,3], S. Rutchantuek[4] and M. Geso[1]

*[1] Department of Medical Radiation, School of Health and Biomedical Sciences, RMIT University, Bundoora, Australia*
*[2] Division of Particle Radiation Medical Physics, Institute for Integrated Radiation and Nuclear Science, Kyoto University, Japan*
*[3] Division of Radiation Therapy, Kita-Harima Medical Center, Hyogo, Japan*
*[4] Department of Diagnostic and Therapeutic Radiology, Faculty of Medicine, Ramathibodi Hospital, Mahidol University, Bangkok, Thailand*

**INTRODUCTION:** Alanine dosimeters are organic crystalline amino acids ($C_3H_7NO_2$) that produce a stable free radical upon their irradiation. The concentration of these generated free radicals is proportional to the absorbed dose which can be determined by electron paramagnetic resonance (EPR) spectroscopy. Alanine is water-equivalent (density 1.42 g/cm³, effective atomic number 6.8) and energy-independent (but only above 100 keV) within the therapeutic range (6-25 MeV). However, the response of alanine to ultra-high-dose-rate of electrons has not been reported yet. This experiment aimed to investigate the energy dependence and response of alanine dosimeters to ultra-high-dose-rate electron beams with energies up to 40 MeV from the Electron Linear accelerator facility, Kyoto University.

**EXPERIMENTS:** Alanine pellets were inserted into a solid water phantom behind a 1 cm buildup phantom and irradiated with electron beams at energies of 9, 20, 30 and 40 MeV, with pulse dose rates up to $10^6$ Gy/s, with pulse duration of 200 ns, and doses ranging from 8, 10, 15, 20, to 30 Gy. The EBT-XD films were placed in front of the alanine pellets during irradiation to verify beam position and validate dose delivery. The energy dependence was evaluated by comparing the relative response of the EPR signal from alanine dosimeters with electron-beam irradiation to that with a Co-60 gamma reference beam (doses 2-50 Gy).

**RESULTS:** As shown in Fig. 1, alanine dosimeters demonstrated a linear EPR dose response with no significant energy dependence for electron beams over the 9 to 40 MeV energy range. We are currently drafting the results for publication.

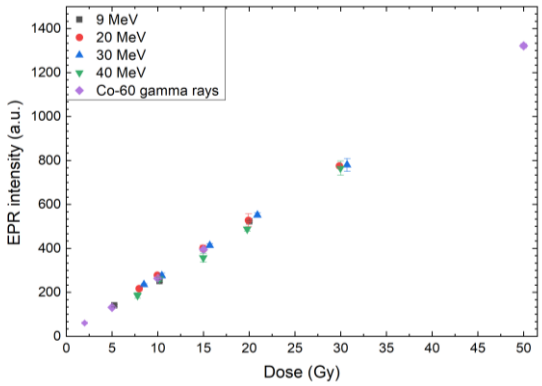


Fig.1. EPR signal amplitude obtained from alanine dosimeter irradiated with 9, 20, 30 and 40 MeV electron beam and Co-60 gamma ray.

**REFERENCES:**

[1] D.F. Regulla and U. Deffner, Int. J. Appl. Radiat. Isot. **33**(1982) 1101–1114.
[2] Anton, M., et al., . Phys Med Biol, 2013. **58**(10): 3259-3282.
[3] H. Kudoh, et al., Appl. Radiat. Isot.,. **48**(1997): 497–499.

## CO6-4

# Elucidation of the As(III)-specific aggregation process of the novel identified As(III)-aggregating protein GatB

S. Kawai-Noma[1], C. Goto[1], K. Otsuka[1], T. Niwa[2], Y. Tanaka[3], T. Saito[1], N. Suda[1], T. Morishima[4], M. Shimizu[4], A. Ito[5], S. Ogasawara[5], T. Murata[5], M. Sugiyama[4], K. Kamiya[5], S. Yagai[6], Y. Ogra[3], and H. Taguchi[2]

*[1] Chiba Univ. Grad. Sch. Eng.[1] Cell Biol. Cent., Inst. Sci. Tokyo[2], Chiba Univ. Grad. Sch. Pharm. Sci.[3], Kyoto Univ., KURNS[4], Chiba Univ. Grad. Sch. Sci.[5], Kanagawa Inst. Technol. Cent. Liberal Arts Sci. Educ7, Chiba Univ. Inst. Adv. Acad. Res.[6]*

**INTRODUCTION:** Trivalent arsenic [As(III)] is highly toxic and can induce protein aggregation by binding to thiol groups [1]. However, the properties of As(III)-aggregating proteins and their aggregation mechanisms remain unclear. We previously showed that As(III)-induced aggregation can function as a protein switch [2]. To systematically identify such proteins, we performed a comprehensive LC-MS/MS analysis of approximately 4,000 proteins in *Escherichia coli*. We identified 23 candidates and confirmed eight as As(III)-aggregating proteins after purification and individual evaluation. Among them, GatB exhibited the strongest aggregation. This study aimed to elucidate the molecular mechanism of the As(III)-specific aggregation process of GatB through physicochemical analyses.

**EXPERIMENTS:** To identify the As(III)-binding site of GatB, mutants were generated in which the putative reactive cysteine residue (C9) was replaced with serine, threonine, or histidine (C9S, C9T, and C9H). Each mutant and wild-type GatB were purified using Ni-NTA Sepharose, followed by the addition of As(III) to a final concentration of 62.5 ppm and incubation at room temperature for 24 h. Time-dependent changes in molecular assembly size upon As(III) binding were analyzed using DLS (dynamic light scattering), AUC (analytical ultracentrifugation), and SAXS (small-angle X-ray scattering).

**RESULTS:** Evaluation of As(III)-induced aggregation behavior and As(III) binding of GatB by SDS-PAGE and ICP-MS showed that both the amount of protein and the amount of As(III) in the precipitated fraction increased, suggesting that As(III) was incorporated into the aggregates together with GatB. In the mutants, both the protein amount and the As(III) amount in the precipitated fraction were markedly decreased compared with those in the wild type, indicating that C9 is involved in As(III)-dependent aggregate formation. Moreover, time-course measurements of molecular assembly size by DLS, AUC, and SAXS revealed that GatB aggregates stepwise from monomers to oligomers and eventually to large aggregates upon As(III) binding. Furthermore, MD simulation predicted that As(III) binds to GatB in a bridging manner between C9 and C39, resulting in an increased solvent-exposed surface area of hydrophobic residues. Taken together, these findings suggest that As(III) binding induces hydrophobic interactions, thereby triggering GatB aggregation.

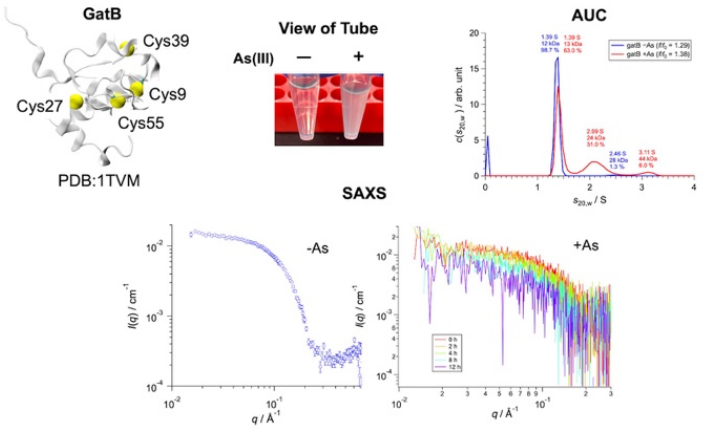


**REFERENCES:**

[1] T. Jacobson, et al., *J. Cell Sci.*, **125** (2012).
[2] Rina Ayuba, et al., *J. Biosci. Bioeng.*, **133**(4) (2022).

CO6-5

# Characterization of transthyretin 49-127 fragment protofibrils by small-angle X-ray scattering combined with analytical ultracentrifugation

Y. Masuda[1], K. Morishima[2], R. Inoue[2], M. Sugiyama[2], E. Chatani[1]

[1] *Graduate School of Science, Kobe University*
[2] *Institute for Integrated Radiation and Nuclear Science, Kyoto University*

**INTRODUCTION:** Amyloid fibrils are needle-like protein aggregates associated with various amyloidosis and neurodegenerative diseases. The plasma protein transthyretin (TTR) is a representative amyloid-forming protein that causes TTR amyloidosis. An N-terminally truncated peptide of TTR, designated as TTR49-127, is recognized as a major constituent of TTR-derived amyloid fibrils. The fibril formation process of TTR49-127 is thought to proceed through the formation of precursor protofibrils, which represent a potential target for therapeutic intervention. In this study, we investigated the structure of these protofibrils using a combination of small-angle X-ray scattering (SAXS) and analytical ultracentrifugation (AUC).

**EXPERIMENTS:** Recombinant TTR49-127 fragment (20 μM) was dissolved in 20 mM phosphate buffer (pH 7.4) containing 100 mM NaCl. To induce protofibril formation, the samples were incubated statically at 37°C for 3 hours. For comparison, mature amyloid fibrils were prepared by incubating the samples at 37°C for 50 hours with continuous agitation at 1200 rpm. The resulting samples were subsequently subjected to SAXS and AUC measurements to evaluate the size distribution and the average shape or size of the aggregates. SAXS measurements were performed at 25 °C with a 30-minute exposure by a NANOPIX equipped with a HyPix-6000 (Rigaku Corporation). The camera length was 1330 mm. A Cu K-α line (MicroMAX-007HFMR) was used as a beam source, which was further focused and collimated with a confocal multilayer mirror (OptiSAXS). AUC data were obtained at 25 °C and 40000 rpm with a ProteomeLab XL-I analytical ultracentrifuge (Beckman Coulter) and analyzed using SEDFIT based on a sedimentation velocity protocol.

**RESULTS:** AUC analysis demonstrated the progression of protofibril formation, revealing that over 80% of TTR49-127 in solution existed as protofibrils. The SAXS profile of the protofibrils (Fig. 1A) exhibited a slope close to −1, indicative of a rod-like morphology, consistent with transmission electron microscopy (TEM) observations [1]. Cross-sectional Guinier analysis estimated the diameter of the protofibrils to be approximately 2.5 nm (Fig. 1B), revealing them to be more than five times thinner than TTR49-127 amyloid fibrils analyzed under the same conditions. Collectively, these results demonstrate that SAXS is a powerful tool for investigating protein aggregates, enabling quantitative characterization of protofibrils.

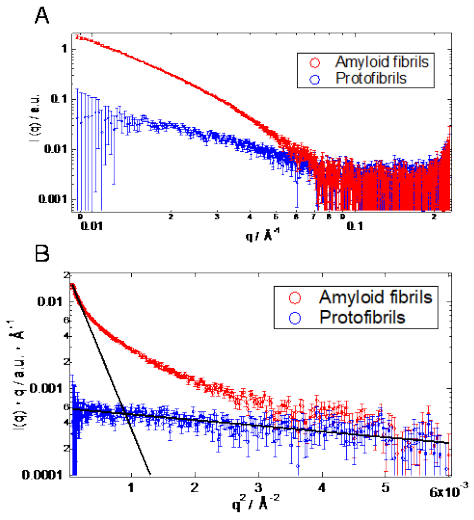


Fig. 1. (A) SAXS profiles and (B) and their cross-sectional Guinier plots of TTR49-127 protofibrils and amyloid fibrils.

**REFERENCE:**
[1] Yuzu et al., *Protein Sci.*, **35**, e70524 (2026).

## CO6-6

# Structural and functional characterization of sHsp from psychrophilic archaeon *Methanococcoides burtonii*

K. Iino[1], K. Morishima[2] , R. Inoue[2], M. Sugiyama[2] and M. Yohda[1]

[1] *Department of Biotechnology and Life Science, Tokyo University of Agriculture and Technology*
[2] *Institute for Integrated Radiation and Nuclear Science, Kyoto University*

**INTRODUCTION:** Small heat shock proteins (sHsps) are widespread low-molecular-weight chaperones that prevent protein aggregation under stress [1]. Under non-stress conditions, they form large oligomers; however, upon stress such as heat, they undergo conformational changes that expose hydrophobic surfaces, enabling them to bind denatured proteins. Generally, heat shock causes large sHsp oligomers to dissociate into smaller forms, making it important to analyze their function and structure in this state. However, typical sHsps from mesophiles become active above 37°C, which complicates their study using standard methods. Therefore, we focused on sHsps from the psychrophilic archaeon *Methanococcoides burtonii*, isolated from the approximately 2°C Ace Lake in Antarctica [3]. *M. burtonii* grows between 0 and 28°C, with an optimal growth temperature of 21°C. Its genome encodes two sHsps, Hsp17.3 and Hsp19.8, which differ in size but both contain an α-crystallin domain typical of sHsps. We expressed Hsp17.3 in *E. coli* and performed its characterization.

**EXPERIMENTS:** The gene for Hsp17.3 was synthesized and cloned into pET23b, then overexpressed in E. coli BL21(DE3). The recombinant Hsp17.3 was purified by anion exchange chromatography followed by gel filtration chromatography, and subjected to functional and structural analyses. Its chaperone activity was evaluated based on its ability to suppress aggregation of reduced lysozyme. The oligomeric state was analyzed by sedimentation velocity analytical ultracentrifugation (SV-AUC).

**RESULTS:** Hsp17.3 was highly expressed in *E. coli* and purified to homogeneity by chromatography. In aggregation suppression assay using reduced lysozyme, Hsp17.3 was able to sufficiently inhibit the aggregation of 30 μM lysozyme even at 15 μM concentration. Thus, Hsp17.3 suppressed lysozyme aggregation at approximately half the molar ratio of the target lysozyme. SV-AUC was used to analyze concentration and temperature dependencies in detail. At concentrations of 2 mg/ml or higher, sharp peaks were detected; however, the sedimentation coefficient varied with temperature. As the temperature in-creased, the apparent molecular weight decreased. At 40°C, the peak intensity diminished, suggesting further dissociation into smaller structures. When the concentration was lowered, the large peak dis-appeared at 40°C, indicating progression of dissociation. At 0.1 mg/ml, almost complete dissociation into dimers or monomers was observed. Association and dissociation of the Hsp17.3 oligomer are dynamic and highly dependent on temperature and concentration.

**REFERENCES:**
[1] C. Garrido *et al.*, Int. J. Biochem. Cell Biol. **44**, (2012), 1588-1592.
[2] M. Haslbeck *et al.*, J. Mol. Biol **427**, (2015), 1537-1548.
[3] P.D. Franzmann, *et al.*, System. Appl. Microbiol. **15**, (1992), 573-581.

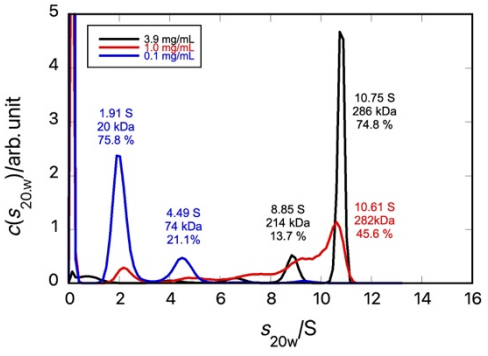


Fig. 1. AUC results of Hsp17.3 at 40°C

# CO6-7

## Physicochemical characterization of amorphous and nanoparticle structures containing poorly water-soluble compounds prepared by spray-freeze-drying

K. Kadota[1], H. Arima-Osonoi [2], T. Okuchi [2],

[1] *Department of Physical Pharmaceutics, Wakayama Medical University*
[2] *Institute for Integrated Radiation and Nuclear Science, Kyoto University*

**INTRODUCTION:** Amorphization and particle size reduction are common strategies to improve drug solubility [1]. This study focuses on wet bead milling to produce stable nanocrystals of mefenamic acid (MFA). We investigated how the type and ratio of polymers (polyvinylpyrrolidone; PVP and hydroxypropyl methylcellulose; HPMC) influence the stability and size of the particles, and compared the performance of these nanocrystals with spray-dried solid dispersions.

**EXPERIMENTS:** MFA suspensions with HPMC or PVP were processed by wet bead milling (UAM-015), while spray-dried samples were prepared for comparison. The physical stability of the samples was monitored for up to 3 months at 40 °C. Powder X-ray diffraction (PXRD) and particle size analysis were used to evaluate changes in crystallinity and particle distribution at specific intervals.

**RESULTS:** Wet bead milling achieved a time-dependent reduction in the particle size of MFA, with the milling rate significantly influenced by the polymer type and concentration; specifically, higher HPMC content (5:1) slowed the milling rate compared to the 3:10 ratio, while PVP formulations required larger 0.3 mm beads to achieve effective reduction (~300 nm) at a 5:1 ratio. Although all formulations initially showed a decrease in crystallinity, stability studies revealed a clear distinction between the two polymers: HPMC-stabilized nanocrystals remained as free-flowing powders even under high humidity (40 °C/75% RH), whereas PVP-containing samples suffered from moisture-induced aggregation, limiting further analysis to sealed, dry conditions. **Figure 1** shows the PXRD patterns of HPMC-based and PVP-based formulations. According to PXRD analysis, HPMC formulations maintained stable crystallinity regardless of particle size, yet the 3:10 ratio exhibited poor redispersibility and significant sedimentation after two weeks of storage. In contrast, the over-milled PVP 3:10 samples showed an increase in crystallinity after one month. Overall, maintaining samples as suspensions resulted in better particle size stability compared to freeze-dried powders, confirming that the milling behavior and subsequent stability of MFA are highly dependent on the specific polymer-drug composition. These underlying molecular mechanisms will be discussed in detail during the presentation.

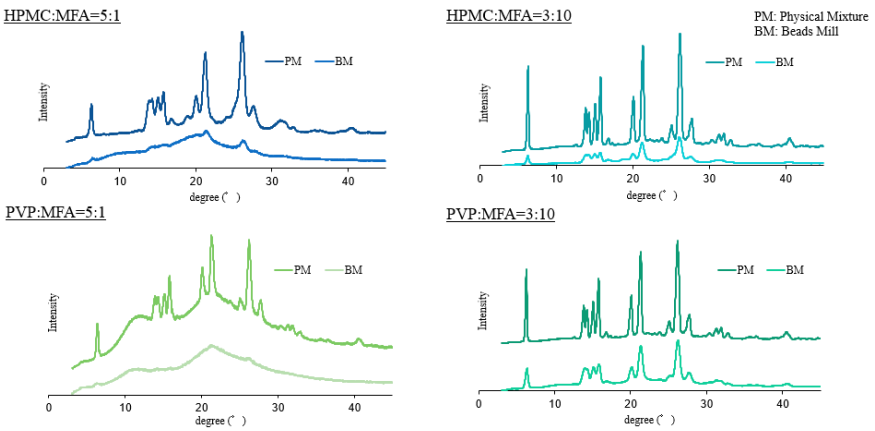


Fig.1 PXRD patterns of HPMC-based and PVP-based formulations.

**REFERENCES:**

[1] Semba K, et al., Improved water dispersibility and photostability in folic acid nanoparticles with transglycosylated naringin using combined processes of wet-milling and freeze-drying, Food Res Int., 121, 108-116 (2019).

# CO6-8

## Investiation of protein domain motion of PGK through AUC-SAXS measurement and MD simulation

T. Oroguchi[1], R. Inoue [2], K. Morishima[2], M. Sugiyama[2]

[1] *Department of Physics, Faculty of Science and Technology, Keio University*
[2] *Institute for Integrated Radiation and Nuclear Science, Kyoto University*

**INTRODUCTION:** Biomolecules are natural nanomachines that perform their functions through dynamic motions in solution. Therefore, to understand the molecular mechanisms underlying biomolecular function, it is essential to visualize these motions at atomic resolution. We have succeeded in achieving such visualization by developing the manifold-based gradient method (MBGD), which integrates SAXS data with molecular dynamics (MD) simulations [1]. By applying MBGD to several proteins undergoing domain motions, we have investigated the mechanisms by which protein motions give rise to biological function.

In this year, we focused on phosphoglycerate kinase (PGK) as a representative protein exhibiting such domain motions. We performed AUC-SAXS measurements of PGK and compared the experimentally inferred motions with those observed in MD simulations.

**********

**EXPERIMENTS:** The PGK sample was loaded onto a size-exclusion chromatography column to obtain a monodisperse protein fraction. After confirming by AUC that the purified PGK was present entirely in the monomeric state, SAXS measurements were performed at a protein concentration of 4 mg/mL at 293 K. The resulting SAXS data were then compared with a 1-μs MD simulation carried out at 293 K.

**********

**RESULTS:** During the 1-μs MD simulation, PGK exhibited an opening–closing domain motion between its domains (Fig. 1A), and the calculated SAXS profile changed depending on this domain motion. A significant difference was observed between the SAXS profile calculated from the MD-derived conformational ensemble (Fig. 1B) and the experimental SAXS profile (Fig. 1C). For example, the radius of gyration estimated from the MD-derived SAXS data was 24.7 Å, whereas that obtained from the experimental SAXS data was 24 Å, indicating that PGK adopts a more compact structure in solution than predicted by the MD simulation.

These results suggest that the inter-domain interactions acting in the MD simulation are weaker than those in the actual solution state. The present SAXS data therefore provide useful experimental information for refining the molecular interactions used in MD simulations.

**********

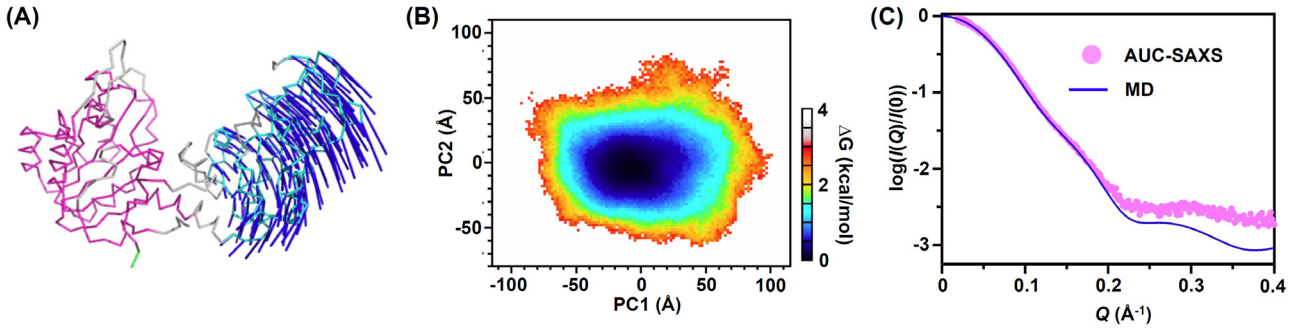


Fig. 1 (A) Domain motion of PGD observed in the 1-μs MD simulation. (B) MD-derived conformational ensemble projected on the two PC modes. (C) Comparison between experimental (pink) and MD-derived SAXS data.

**REFERENCES:**

[1] T. Oroguchi, *et al.*,. arXiv ID: 2410.01499 (2025)

## CO6-9

# Tracking structural growth of transthyretin protofibrils using analytical ultracentrifugation

N. Yamamoto[1], K. Morishima [2], R. Inoue [2], E. Chatani[3] and M. Sugiyama[2]

[1] *School of Medicine, Jichi Medical University*
[2] *Institute for Integrated Radiation and Nuclear Science, Kyoto University*
[3] *Graduate School of Science, Kobe University*

**INTRODUCTION:** Transthyretin (TTR) is a plasma protein carrying small molecules such as thyroxine and retinol. Its amyloid fibril formation is related to systemic amyloidosis known as ATTR, where the fibrils accumulate in organs such as the heart, leading to their dysfunction. Understanding the formation mechanism is thus essential for finding ways to treat the disease. Protofibrils are one of the key species accumulating prior to the amyloid fibril formation. We have recently found that TTR forms protofibrils in an acidic condition [1]. In this study, we tracked structural growth of the protofibrils using analytical ultracentrifugation (AUC).

**EXPERIMENTS:** TTR at the concentration of 100 μM in 10 mM HCl and 100 mM NaCl was incubated at 75 °C, and sampled at appropriate time points for AUC experiments. AUC was performed at 25 °C using XL-I (Beckman Coulter, Indiana).

**RESULTS:** Fig. 1 shows the time dependence of AUC profiles. Immediately after the reaction started (0 h), one peak at ~250 kDa was observed, indicating the emergence of aggregates. Several amorphous aggregates were confirmed in the TEM images (Fig. 2, 0 h). These aggregates were identified as oligomers. At 1 h, the AUC profile was largely unchanged from that at 0 h (Fig. 1D, 1 h). In contrast, at 16 h, a broad peak appeared at ~1,300 kDa in addition to a peak at ~250 kDa (Fig. 1, 16 h). Curvy components were observed in the TEM images (Fig. 2E, 16 h), corresponding to protofibrils. Both the proportion and the molecular weight of the protofibrils increased as a function of time (Fig. 1, 16, 24, 36, and 48 h), indicating protofibril elongation during formation. The elongation was also confirmed by the TEM image (Fig. 2, 48 h).

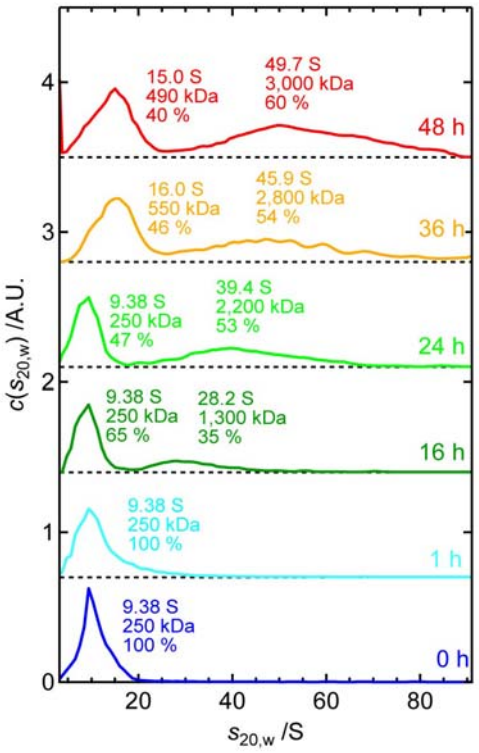


Fig. 1. Time-dependent AUC profiles. The sedimentation coefficient, molecular weight, and population of each component are shown.

**REFERENCES:**

[1] N. Yamamoto, K. Morishima, R. Inoue, M. Sugiyama, and E. Chatani. *Manuscript in revision*.

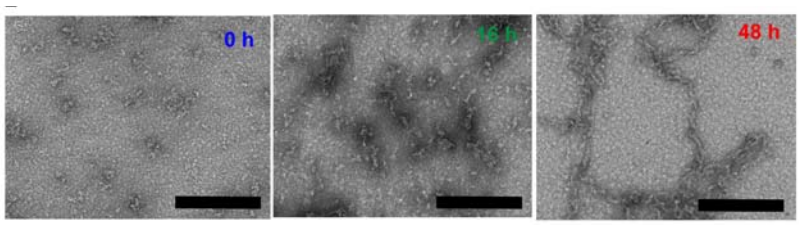


Fig. 2. Negatively-stained TEM images acquired at several time points. The scale bar indicates 200 nm.

## CO6-10

# 2D-Mapping Image of Tumor Model Dried Tissue in the Sub-THz Region

N. Miyoshi[1], H. Sato[2], B. B. Andriana[2], and T. Takahashi[3]

[1]*Department of Cellular Immunology, Graduate School of Medical Sciences, Nagasaki University.*
[2]*Department of Life Sciences, Graduate School of Life Environment, Kwansei-Gakuin University.*
[3] *Institute for Integrated Radiation and Nuclear Science, Kyoto University*

**INTRODUCTION:** Spectroscopic analysis in the sub-THz region within the field of tumor pathology is of interest from the perspective of water interactions and is important for understanding hydrogen bonding in the context of MRI.

**EXPERIMENTS:** The experiment was performed using KURNS-LINAC. The electron beam energy was 39 MeV, and the average beam current was 1.9 μA. The macro-pulse repetition rate was 60 pulses/s. Coherent transition radiation (CTR) from a titanium window was guided to a Fourier transform interferometer in the experimental room via a coherent radiation beamline [1]. A liquid-helium-cooled silicon bolometer was used as the CTR detector. The sample was prepared as a tumor model using cancer drugs at Kwansei-Gakuin University. The sample tissue was sandwiched between two 0.5-mm-thick PVC plates, as shown in Fig. 1.

**RESULTS:** In a previous study [2], we observed absorption in the tumor area within the spectral region of 11 to 16 $cm^{-1}$. Figure 2 shows the measurement area for the 2D-mapping image (indicated by the red square). The resulting mapping image is shown in Fig. 3. It was possible to identify the regions of tumor and normal tissues from this image.

**REFERENCES:**

[1] T. Takahashi et al., Rev. Sci. Instrum. 69 (1998) 3770.
[2] N. Miyoshi et al., KURNS Progress Report 2024 CO6-10.

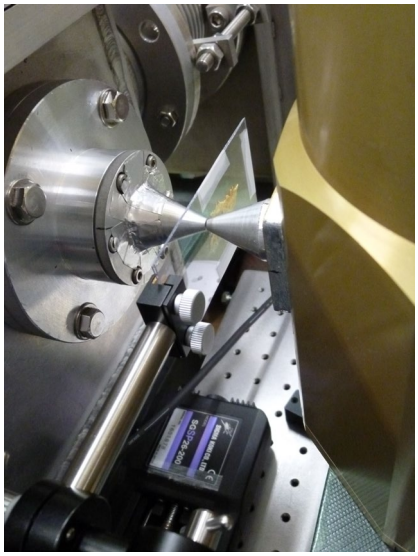

Fig. 1 Experimental setup of the sample.

Fig. 2 Measurement area of 2D-mapping image (square).

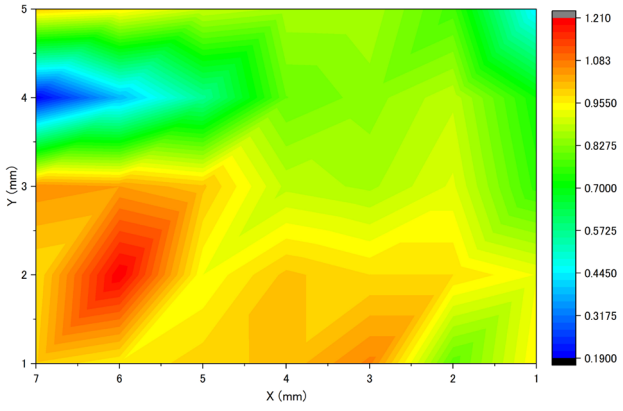


Fig. 3 2D-mapping image of transmittivity in the spectral region from 11 to 16 $cm^{-1}$.

# CO6-11

## Smaller oligomers-distributions of hnRNPA2 low-complexity domain by analytical ultracentrifugation measurements

E. Mori[1], N. Iguchi[2], N. Isozumi[1], K. Morishima[3] and M. Sugiyama[3]

[1] *Department of Future Basic Medicine, Nara Medical University, Kashihara, Nara, Japan*
[2] *Department of Neurology, Nara Medical University, Kashihara, Nara, Japan*
[3] *Institute for Integrated Radiation and Nuclear Science, Kyoto University, Kumatori, Sennan-gun, Osaka, Japan*

**INTRODUCTION:** Proteins with sequence low-complexity (LC domains) have potential to self-associate and play important roles in molecular crowding, called phase separation. Human genetics revealed that patient-derived mutations have impacts on biophysical properties of LC domains, and the F/Y to S mutation in LC domain of hnRNPA2 (A2-LC) has been reported to suppress polymer formation [1]. To monitor a monomeric state and a polymeric state, we compared different mutants of (A2-LC).

**EXPERIMENTS:** We prepared mCherry-tagged A2-LC (residues 181-341) (mCh:A2-LC) with F291S mutant (A2-LC_F291S), which is a representative mutant known to suppress polymer formation, and a A2-LC mutant (A2-LC_MM) in which multiple F/Y residues were mutated to S (Y257S, Y264S, Y278S, F291S, F309S, and Y319S). All mCherry fusion proteins were expressed in *E. coli* BL21(DE3) cells with 0.5 mM IPTG. Analytical ultracentrifugation (AUC) measurements were performed with a ProteomeLab XL-I (software version 6.2, Beckman Coulter, USA). All samples were prepared at a concentration of 1.0 mg/mL in a solution containing 20 mM Tris-HCl, pH 7.5, 200 mM NaCl, 20 mM β-ME, and 0.1 mM PMSF. The samples were loaded into a cell with a 12 mm optical-pathlength and were measured using Rayleigh interference optics at a rotor speed of 20,000 rpm and temperature of 25 °C. The time evolution of the sedimentation data was analyzed with Lamm formula using SEDFIT software (version 15.01c) [2]. The weight concentration distribution $c(s_{20,w})$ was obtained as a function of the sedimentation coefficient which was normalized to the value at 20 °C in pure water $s_{20,w}$.

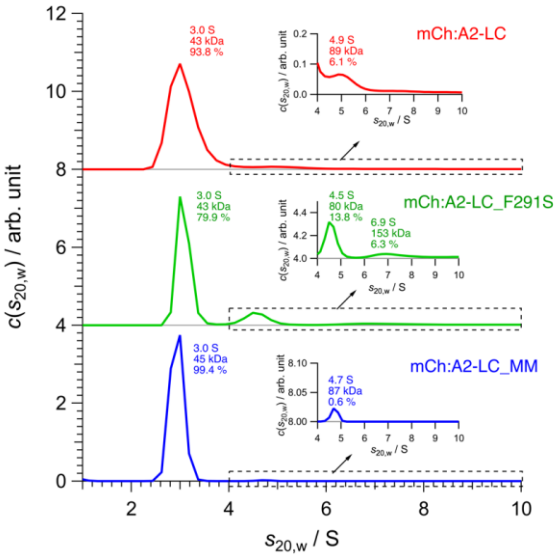


Fig. 1. Smaller oligomers-distributions in mCh:A2-LC samples by AUC measurements. Red, green, and blue lines show the weight concentration distribution $c(s_{20,w})$ for mCh:A2-LC, mCh:A2-LC_F291S, and mCh:A2-LC_MM, respectively. Sedimentation coefficient, molecular mass, and weight fraction for each peak are noted in the figure.

**RESULTS:** As shown in Fig. 1, AUC for mCh:A2-LC, mCh:A2-LC_F291S, and mCh:A2-LC_MM showed the presence of not only monomers but also dimers (and trimers for mCh:A2-LC_F291S). The weight fractions of dimers and trimers for mCh:A2-LC and mCh:A2-LC_F291S were higher than that for mCh:A2-LC_MM, suggesting a stronger tendency for association.

**REFERENCES:**

[1] S. Xiang *et al*., Cell, **163** (2015) 829-839.
[2] P. Schuck *et al*., Biophys. J., **82** (2002) 1096-1111.

# CO6-12

## Evaluation of oxidized lens βB2-crystallins involved in age-related cataract

T. Takata[1], J. Sun[2], D. Sasaki[2] and K. Lampi[3]

[1] *Institute for Integrated Radiation and Nuclear Science, Kyoto University*
[2] *Dept of Chemistry, Graduate School of Science, Kyoto University*
[3] *Oregon Health & Science University*

**INTRODUCTION:** The transparency of the lens is maintained by the stable long-lived protein interactions, comprising three kinds of crystallin families. Those proteins are very stable, but are decreased their stability with age. A kind of intrinsic damages of lens crystallins, such as heat damage, or extrinsic damages such as UV damage are increased with life time. Several researches suggested the amount of UV damage on lens crystallins could be well described by the amount of modifications of amino acid residues [1]. Oxidation of tryptophan residue (Trp: W) is one of the primary damages for crystallins after heat/UV exposure. Therefore, we made oxidation mimic lens βB2-crystallin and investigated those biochemical effect for oligomerization and stabilities. In order to investigate more details, we used those proteins for SAX experiment to compare βB2-crystallin mimic protein with reported structures.

**EXPERIMENTS:** Five tryptophan residues in βB2-crystallin were replaced by phenylalanine residues (Phe: F) respectively to simulate the oxidation effect of Trp in βB2-crystallin by site-directed mutagenesis (W59F, W82F, W85F, W151F and W196F). Each sample were purified and used for the SAXS measurements using by NANOPIX (Rigaku, Japan) at 298 K. The detected two-dimensional scattering patterns were then converted to a one-dimensional scattering profile using circular averaging. An ab initio model was built with a dummy atom method, DAMMIF in the ATSAS software package (version 3.1.3) based on the SAXS profile [2]. 7K7U.pdb and 1OKI.pdb were used to generate SAXS profiles for comparing with the experimental results in this study.

**RESULTS:** SAXS analysis revealed that the βB2-crystallin dimer model in solution resembles the lattice βB1-crystallin dimer (Fig. 1a and 1b), while the tetramer model from resembles its lattice tetramer (data not shown). The W→F mutations did not significantly alter the shape of each homo-oligomer; however, the distribution of oligomeric states differed among the mutants. These results suggest that oxidation affects the homo-oligomer assembly of crystallin without dramatically altering its overall structure. Notably, W59F showed an increased proportion of tetramers and decreased thermal stability, indicating that the effects of oxidation are complex rather than uniform. Through these experiments, we were able to obtain insights into the effects of oxidative modification of tryptophan residues—one of the initial focuses of this year's plan—on the homo-oligomeric structure of βB2-crystallin. On the other hand, βB2-crystallin is known to form hetero-oligomers with βA3-crystallin, a partner subunit in the lens [3]. Therefore, in future work, we aim to investigate the hetero-oligomerization ability of the oxidized βB2-crystallin generated in this study with βA3-crystallin, as well as to analyze their structures.

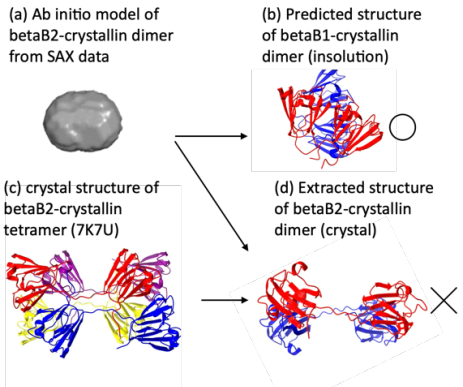


Fig. 1. Superposition of betaB2-crystallin dimer ab initio model and betaB1-crystallin dimer/ extracted structure of betaB2-crystallin dimer.

**REFERENCES:**

[1] B. Searle *et al.*, J Proteome Res, **4** (2005) 546-554
[2] D. Franke D et al., J Appl Crystallogr. **42** (2009) 342–346.
[3] A. Rolland *et al.*, Structure. **31** (2023) 1052–1064.

## CO6-13

# $^{11}$C Medical-isotope Production via $^{12}$C(γ,n)$^{11}$C Reaction with Carbon Nanorings

N. Takahashi[1,2], M. Kurosawa[1], M. Tamura[1], M. Fujiwara[1,2], T. Kubota[3], N. Abe[4], and T. Takahashi[4]

[1]*Research Center for Nuclear Physics, Osaka University*
[2]*Kyoto Medical Technology*
[3]*Agency for Health, Safety and Environment, Kyoto University*
[4]*Institute for Integrated Radiation and Nuclear Science, Kyoto University*

**INTRODUCTION:** L-[$^{11}$C]-Methionine is employed as a reagent for PET imaging to diagnose brain tumors [1]. The medical $^{11}$C radioisotopes are mostly produced in a cyclotron via the $^{14}$N(p,α)$^{11}$C reaction by bombarding nitrogen gas with a proton beam [2]. Instead of producing $^{11}$C with the cyclotron, we developed a novel method of producing $^{11}$C using the bremsstrahlung γ-rays with a carbon nanoring (CNR) to get a reasonable number of the $^{11}$C activity.

**EXPERIMENTS:** Figure 1 shows the experimental scheme for the $^{11}$C production via the $^{12}$C(γ,n)$^{11}$C reaction. Bremsstrahlung γ-rays were produced by impinging a 40 MeV electron beam on platinum converter at the electron LINAC facility. The γ-rays were irradiated to CNR sealed in aluminum vessel with non-woven masks as gas inlet/outlet filter. The produced $^{11}$C inside the vessel were oxidized to $^{11}$CO or $^{11}$CO$_2$ in O$_2$ gas, which was continuously flown during the irradiation. The $^{11}$C gas ($^{11}$CO and $^{11}$CO$_2$) were trapped in two 13X molecular sieve columns. 511-keV γ-rays from positron-electron annihilation were detected with CdZnTe detectors. The CNR with a diameter of 0.8nm ($C_{36}H_{24}$) and 1.6 nm ($C_{72}H_{48}$) were used as target.

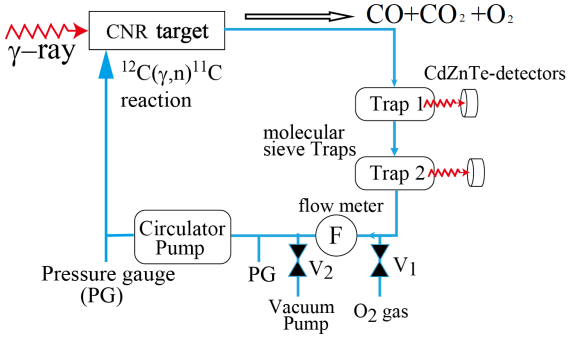


Fig. 1 Experimental scheme to produce $^{11}$C and measure the extraction rate of $^{11}$C gas.

**RESULTS:** Table 1 shows the normalized activity of $^{11}$C gas for $C_{36}H_{24}$ and $C_{72}H_{48}$. The normalized activity for $C_{72}H_{48}$ was about two times higher than that for $C_{36}H_{24}$.

Based on the experimental production rate of $^{11}$C gas, we estimate that we can obtain the $^{11}$C activity of 117 GBq when we use a $C_{72}H_{48}$ target under the conditions with 1) a length of 50 cm, 2) weight of 1.13 kg for 0.155 g/cm$^3$, 3) a 40 MeV electron beam intensity of 100 μA for 40 minutes bombardment.

Table 1 Normalized activity of $^{11}$C gas for each type of target

| Type of target | Normalized activity of $^{11}$C gas (kBq/μA/g/min) |
|---|---|
| CNR ($C_{36}H_{24}$) | 14.74±0.09 |
| CNR ($C_{72}H_{48}$) | 29.11±0.08 |

**REFERENCES:**

[1] Kobayashi K. *et al.*, Eur. J. Nucl. Med. Mol. Imaging, **42** (2015) 1071-1080.
[2] David R. Christman *et al.*, Int. J. appl. radiat. isot. **26** (1975) 435-442.

# CO6-14

## Investigation of the Biological Impact of Ultra-High Dose Rate Radiation on Normal and Neoplastic Tissues

T. Watanabe[1], G. E. Sato[1], T. Takata[2], Y. Sakurai[2], M.Suzuki[1], T.Mizowaki[3], H. Tanaka[2]

*Institute for Integrated Radiation and Nuclear Science, Kyoto University*
*[1]Particle Radiation Oncology Research Center, Particle Radiation Oncology*
*[2]Particle Radiation Oncology Research Center, Particle Radiation Medical Physics*
*[3]Kyoto Univeristy, Department of Radiation Oncology and Image-Applied Therapy*

**INTRODUCTION:** Recent studies suggest that ultra-high dose rate irradiation (≥40 Gy/sec), which is over 1,000 times faster than conventional radiotherapy (≈0.03 Gy/sec), may reduce side effects while maintaining comparable anti-tumor efficacy [1]. Radiation with different dose rates is known to have different effects on normal tissues [2]. On the other hand, the effect of dose rate on the antitumor effect is minor, and a higher dose rate may improve the therapeutic efficacy ratio of radiation [3]. The purpose of this study is to ascertain whether the dose rate alters the effects of various normal tissues. In addition, experiments were conducted to see if the antitumor effect of radiation could be differentiated by differences in dose rate, which had previously been equivalent, by using drugs that affect the antitumor effect of radiation in combination.
**********

**EXPERIMENTS:** We aim to clarify the effects of high-dose rate irradiation—which exhibits distinct biological responses compared to conventional X-ray irradiation—on lymphocytes. First, we established in vivo/in vitro irradiation systems for high-dose-rate exposure using electron beams. Next, we administered high-dose-rate irradiation to the head and neck regions of C3H and C57/BL6 mice, confirming that dermatitis in the high-dose-rate group was reduced compared to the conventional dose-rate group, consistent with published reports. Furthermore, lymphocytes isolated from the spleens of C3H mice were irradiated with 0, 2, 4, and 10 Gy using both conventional and high-dose-rate methods. Based on literature indicating the critical role of oxygen concentration in high-dose rate effects, irradiations were conducted under in vitro conditions with varying oxygen levels. Subsequently, using 5% oxygen conditions (validated for high-dose rate effects in mouse skin), additional irradiations of 0, 4, and 10 Gy were performed under both 1% and 5% oxygen conditions.
**********

**RESULTS:** High-dose-rate irradiation to the head and neck regions of C3H and C57/BL6 mice confirmed that dermatitis was reduced in the high-dose-rate group compared to the conventional dose-rate group, consistent with prior reports. Under 0.1% oxygen conditions, no difference in lymphocyte survival rates was observed between high-dose-rate and X-ray irradiation, and no high-dose rate effect was detected at this oxygen level. Using 5% oxygen conditions (previously validated for high-dose rate effects in mouse skin), 0, 4, and 10 Gy irradiations were repeated under both 1% and 5% oxygen levels. However, under all conditions, no irradiation method-dependent differences in lymphocyte survival rates were observed, and in vitro experiments showed no high-dose rate effect regardless of oxygen concentration.
**********

**REFERENCES:**

[1] JD Wilson et al. Front Oncol (2020) DOI: 10.3389/fonc.2019.01563
[2] Binwei Lin, Feng Gao, Yiwei Yang, Dai Wu, Yu Zhang, Gang Feng, Tangzhi Dai, and Xiaobo Du. Front Oncol., 11 (2021) 644400.
[3] Elise Konradsson, Emma Liljedhal, Emma Gustafsson, Gabriel Adrian, Sarah Beyer, Suhayb Ehsaan Ilaahi, Kristoffer Petersson, Crister Ceberg, Henrietta Nittby Redebrandt. Advances in Radiation Oncology., 7 (2022) 101011.

# CO6-15

## Association kinetics of circadian Kai-protein complex in solution

K. Morishima, Y. Katsuno, and M. Sugiyama

*Institute for Integrated Radiation and Nuclear Science, Kyoto University*

**INTRODUCTION:**

Cyanobacterial circadian oscillations arise from complex formation among KaiA, KaiB, and KaiC, coupled to the phosphorylation cycle of KaiC. While the formation of KaiA–KaiC (AC) and KaiB–KaiC (BC) complexes has been characterized, understanding how KaiA associates with the preformed BC complex is essential for clarifying the dynamic regulation of the oscillator.

In particular, once the $B_6C_6$ is formed, KaiA binding leads to the formation of ABC complexes with variable stoichiometry ($A_nB_6C_6$). In this study, we focus on the kinetics of KaiA association to preformed $B_6C_6$ complexes using time-resolved small-angle X-ray scattering (SAXS) [1]. The aim is to directly observe how the ABC complex forms and reaches equilibrium immediately after mixing.

**EXPERIMENTS:**

$B_6C_6$ was prepared by mixing KaiB and $KaiC_{DE}$ (hyperphosphorylation S431D/T432E mutant) at a molar ratio of [KaiB] : [KaiC] = 6 : 6, followed by incubation at 30 °C for 24 hours and purification by size exclusion chromatography. KaiA was added to the preformed $B_6C_6$ solution at a defined mixing ratio of [A] : [$B_6C_6$] = 6 : 1.

SAXS measurements were performed immediately after mixing KaiA and $B_6C_6$ at 30 °C using a laboratory SAXS instrument (NANOPIX, Rigaku). Scattering profiles were collected at 2-min intervals immediately after mixing. The scattering intensity was analyzed using Guinier approximation to obtain the forward scattering intensity $I(0)$, which reflects the molecular assembly state.

**RESULTS:**

Immediately after mixing KaiA with $B_6C_6$, the $I(0)$ reached a constant value within the first measurement time point ($\leq$ 2 min) (Fig. 1). The $I(0)$ value agreed well with the calculated value expected for the $A_6B_6C_6$ complex, rather than a mixture of $B_6C_6$ and $A_{12}B_6C_6$. This indicates that KaiA is not forming a fully saturated $A_{12}B_6C_6$, but instead distributes evenly among $B_6C_6$ to form $A_nB_6C_6$. Such rapid redistribution implies that KaiA occupancy in ABC complexes is dynamically determined by the mixing ratio rather than fixed stoichiometry. This mechanism enables flexible allocation of KaiA among complexes, which is likely essential for maintaining robust circadian oscillations under fluctuating conditions.

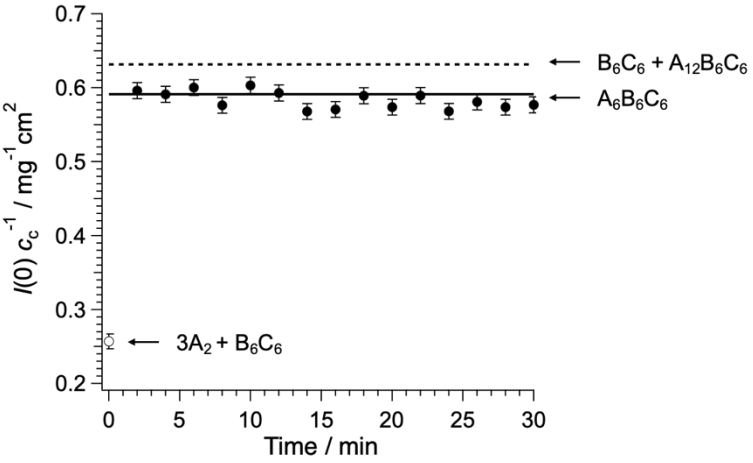


Fig. 1. Closed circles represent the forward scattering intensity normalized by KaiC-concentration ($I(0)c_c^{-1}$) provided by the time-resolved SAXS after mixing KaiA and $B_6C_6$. Open circle is the values for the dissociated ($A_2$ and $B_6C_6$) state. Solid line corresponds to the calculated $I(0)c_c^{-1}$-value for $A_6B_6C_6$. Broken black line corresponds to that for the summation of $B_6C_6$ and $A_{12}B_6C_6$, respectively.

**REFERENCES:**

[1] K. Morishima, *et al.*, BioRxiv (2026). doi:10.64898/2026.03.06.710049v1.

# CO6-16

## Site-specific deuteration of multi-domain proteins for small angle neutron scattering

T. Oda[1], R. Inoue[2], K. Morishima[2], A. Okuda[2], C. Shibazaki[1], M. Sugiyama[2]

[1]*J-PARC Center, Japan Atomic Energy Agency.*
[2]*Institute for Integrated Radiation and Nuclear Science, Kyoto University.*

**INTRODUCTION:** Small-angle X-ray scattering (SAXS) provides structural ensembles of proteins in solution. By comparing these profiles with molecular dynamics (MD) simulations, the dynamics of flexible multi-domain proteins can be analyzed. However, SAXS data interpretation remains ambiguous as it yields only a single curve for the entire molecule. Conversely, small-angle neutron scattering (SANS) with site-specific deuteration can significantly reduce this uncertainty by isolating scattering from specific domains. Despite its potential, preparing such samples remains technically challenging. Specifically, these samples are prepared by ligating protonated and deuterated fragments using ligation enzymes. Using the multi-domain protein Hef—which consists of N-terminal helicase and C-terminal nuclease domains connected by an intrinsically disordered region (IDR) [1,2]—as a model, we previously succeeded in selectively deuterating either only the N- or C-terminal domain using NpuDnaE as a ligation enzyme (Fig 1 a,b). Here, we aimed to prepare a Hef sample where both terminal domains are exclusively deuterated (Fig 1c), leaving only the central IDR protonated to selectively observe its scattering profile.

**EXPERIMENTS:** Ligation efficiency depends on the enzyme type and steric hindrance at the target site. While NpuDnaE was used for the IDR and C-terminal domain, we screened three enzymes at two positions (six patterns total) to optimize the N-terminal–IDR ligation (Fig 1c). These small-scale tests were performed using non-deuterated proteins to identify the most efficient combination for subsequent large-scale preparation.

**RESULTS:** Small-scale screening identified a single successful combination using OaAEP. Applying this to site-specific deuteration, we utilized 2 L of deuterated culture for each terminal domain and 2 L of non-deuterated culture for the IDR. This process successfully yielded 1.5 mg of the final site-specifically deuterated Hef protein (Fig 1d).

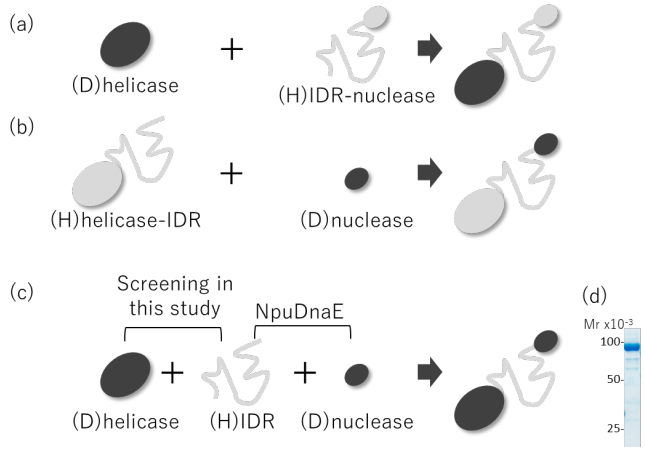


Fig 1. Schematic representation of site-specific deuteration strategies for Hef. (a, b) Preparation of Hef samples with either the N-terminal or C-terminal domain selectively deuterated. (c) Strategy for preparing the site-specifically deuterated Hef where both terminal domains are deuterated while the central IDR remains protonated. The ligation between IDR and nuclease was performed using NpuDnaE, whereas the ligation between helicase and IDR was optimized through screening in this study. (d) SDS-PAGE analysis of the final purified product (c) after ligation and purification.

**REFERENCES:**

[1] Fujikane et al, (2010) Genes Genet. Syst. 85, 243.
[2] Ishino et al, (2014) J. Biol. Chem. 289, 21627.

# CO6-17

## Distribution analysis of the chemical modification of the amino acid residues in lens structural proteins during age-related cataract

S. Matsushita[1], Y. Suzuki[1], A Ohtani[1], M. Yurugi[2] and T. Takata[3]

[1] *Dept of Materials and Applied Chemistry, Nihon University*
[2] *Dept of Chemistry, Kyoto University*
[3] *Institute for Integrated Radiation and Nuclear Science, Kyoto University*

**INTRODUCTION:** Age-related cataracts are a leading cause of blindness worldwide. Several risk factors contributing to cataract development have been identified, among which abnormal aggregation and insolubilization of lens proteins are considered primary mechanisms. Structural alterations induced by covalent post-translational modifications play a critical role in lens protein homeostasis [1]. We have previously demonstrated that such modifications can serve as markers of lens aging. Although mass spectrometry is a powerful tool for quantitative analysis, the spatial distribution of these modifications remains unclear. In this study, we aim to elucidate the distribution of modifications, particularly isomerization and racemization of Asp residues, in lens sections using imaging mass spectrometry (IMS) [2]. To facilitate this analysis, we examined model peptides on a sample plate with a matrix solution to identify peptides based on their molecular mass.

**EXPERIMENTS:** Model peptides derived from lens proteins were synthesized, purified, and mixed with either CHCA ((4-hydroxyphenyl) acrylic acid) or DHB (2,5-dihydroxybenzoic acid) as matrices for MALDI-TOF MS in 50% acetonitrile. Modification sites (L-α-Asp, L-β-Asp, D-α-Asp, and D-β-Asp) were confirmed by LC-MS/MS at the Kyoto University Institute for Integrated Radiation and Nuclear Science. Samples were mixed with matrixes and loaded onto an imaging plate at three peptide concentrations. Data were acquired in positive ion mode (*m/z* 100–2500) using a JMS-S3000 (JEOL), and a peak at *m/z* 1311.70–1312.05 was observed (Fig. 1).

**RESULTS:** The results suggested that peptide concentrations above 1.0 mg/mL produce detectable images for both matrixes. Notably, DHB enabled more stable detection at lower concentrations compared to CHCA. The observed signal patterns were heterogeneous rather than uniform. Drying of droplets containing the peptide–matrix mixture can generate debris on the plate, non-uniform crystallization which interferes with precise quantitative analysis. The ion distribution images obtained by IMS reflect the signal intensity of ions with a specific mass-to-charge ratio (*m/z*) at each pixel. By converting these image data into numerical values, the relative abundance of target molecules in the sample was compared. Absolute quantification in IMS is difficult because ion intensity is affected by factors such as matrix crystal state and ionization efficiency. However, among samples prepared and measured under identical conditions, relative comparisons of peptide abundance can be achieved using an index based on pixel count × mean intensity (Integrated Density). This approach enables quantitative evaluation of peptide abundance in addition to spatial localization.

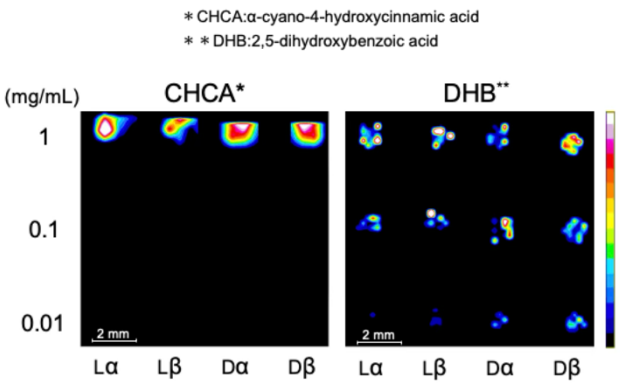


Fig. 1. IMS of lens protein derived peptide containing isomerization/racemization of Asp

**REFERENCES:**
[1] N. Fujii *et al.*, Biochim. Biophys. Acta, **1860** (2016) 183-191.
[2] J. McMahon *et al.*, J. Am. Soc. Mass. Spectrom., **11** (1995) 1047-1058.

# CO6-18

## Micro–Macro Correlations in the Dynamic Structural Properties of Multidomain Proteins

K. Kato[1,2], M. Yagi-Utsumi[1,2], S. Yanaka[1,2,3], H. Yagi[1,2], K. Morishima[4] and M. Sugiyama[4]

[1]*Graduate School of Pharmaceutical Sciences, Nagoya City University*
[2]*Exploratory Research Center on Life and Living Systems (ExCELLS), National Institutes of Natural Sciences*
[3]*Institute of Integrated Research, Institute of Science Tokyo*
[4]*Institute for Integrated Radiation and Nuclear Science, Kyoto University*

**INTRODUCTION:** Multidomain proteins frequently exhibit intrinsic structural flexibility that underlies their biological functions through allosteric regulation and dynamic intermolecular interactions. In particular, antibodies are known to initiate antigen recognition through the Fab region and subsequently activate effector functions through the Fc region. Increasing evidence suggests that antigen recognition and effector activation are dynamically coupled through allosteric communication pathways embedded within the flexible architecture of antibody molecules. Elucidating such dynamic structure–function relationships is essential for understanding biomolecular function and for establishing principles for functional molecular design. In this study, we investigated the solution structural properties of two distinct multidomain protein systems using small-angle X-ray scattering (SAXS) combined with analytical ultracentrifugation (AUC). One system focuses on the allosteric structural response of human immunoglobulin G (IgG) upon interaction with Fcγ receptor IIIb (FcγRIIIb), while the other addresses the dynamic structural properties of nucleobindin proteins (NUCB1 and NUCB2), which are Golgi-associated proteins involved in glycoprotein processing.

**EXPERIMENTS:** SAXS and sedimentation velocity AUC measurements were performed for IgG-related samples and NUCB proteins in solution. For the IgG system, single-arm IgG (sIgG) was analyzed to enhance detection of conformational changes associated with FcγRIIIb binding. For the NUCB system, solution properties of NUCB1, NUCB2, and their mixed samples were examined to characterize conformational heterogeneity and possible oligomerization behavior.

**RESULTS:** For the sIgG/FcγRIIIb system, AUC measurements supported complex formation in solution. Combination of SAXS and AUC analyses enabled extraction of scattering profiles corresponding predominantly to the receptor-bound state while minimizing contributions from free components and aggregates. Structural interpretation of the SAXS data combined with computational modeling is currently in progress. For the NUCB system, AUC analyses suggested no clear formation of stable higher-order oligomers under the examined conditions, while distinct differences in conformational distributions were observed between NUCB1 and NUCB2. SAXS measurements further indicated that NUCB1 exhibited aggregation tendencies, whereas NUCB2 showed solution scattering profiles consistent with relatively expanded conformations. These observations suggest that differences in dynamic conformational properties may contribute to their distinct substrate recognition behaviors. The present study demonstrates the usefulness of SAXS combined with complementary biophysical approaches for characterizing dynamic structural properties of multidomain proteins in solution. Further integration with NMR analyses and computational approaches is expected to provide deeper insights into allosteric regulation and conformational heterogeneity in flexible biomolecular systems.

**REFERENCES:**
[1] K. Koseki *et al.*, J. Med. Chem., **69** (2026) 3902-3914.
[2] H. Yagi *et al.*, iScience **27** (2024) 111457.

# CO6-19

## Aggregation inhibition development based on p53 aggregates analysis

E. Hibino[1], H. Yoshida[2], K. Morishima[3], R. Inoue[3], M. Sugiyama[3] and H. Hiroaki[1,4,5]

[1]*Graduate School of Pharmaceutical Sciences, Nagoya University*
[2]*Department of Biological Science, School of Science, Nagoya University*
[3]*Institute for Integrated Radiation and Nuclear Science, Kyoto University*
[4]*BeCellBar LLC.*
[5]*COMIT*

### INTRODUCTION:

Cancer remains the top cause of death and its incidence rate is also high in Japan. Most anticancer drugs have severe side effects, making treatment a harsh struggle. While molecularly targeted drugs and immune checkpoint inhibitors with significantly reduced side effects have been released in recent years, their applicability is limited to certain types of cancer. In cancer, DNA damage fails to be repaired, causing the bodily systems to function abnormally. Typically, the organism possesses a system that prevents cells from becoming cancerous by repairing DNA damage through the function of tumor suppressor. p53 is one of these factors and is called as the "guardian of the genome" due to its highly effective function. p53 is known to be mutated in about half of all human cancers. Therefore, p53 is a natural anticancer and cancer-preventive drug. In this study, we focused on maintaining the function of p53.

### EXPERIMENTS:

p53-DNA binding domain (DBD) was expressed in an E. coli expression system and purified. The p53-DBD solution was treated with a reagent at various concentrations, incubated at 37°C for 1 h, and then analyzed using various techniques, including Blue Native PAGE, transmission electron microscopy (TEM) observation, and nanoparticle tracking analysis.

### RESULTS:

We performed nanoparticle tracking analysis on the incubated p53-DBD solution without a reagent, with moderate concentration of a reagent, or with high concentration of a reagent (Fig. 1). As a result, numerous particles derived from p53-DBD aggregates were observed in the p53-DBD incubation samples with either no reagent or a high concentration of a reagent. Interestingly, it was shown that aggregation is significantly suppressed at moderate concentrations of a reagent. We hypothesize that the type of aggregates switches upon the addition of a reagent. TEM observations also confirmed the similar results. Furthermore, BN-PAGE experiments revealed bands in the high-molecular-weight region in samples without or with high concentrations of a reagent. However, at a moderate concentration of a reagent, no bands were observed in the high-molecular-weight region, but bands were observed in the relatively low-molecular-weight region. In the future, we will further analyze the molecular structural characteristics of p53-DBD with a moderate-concentration reagent using AUC, DLS, NMR, or SAXS.

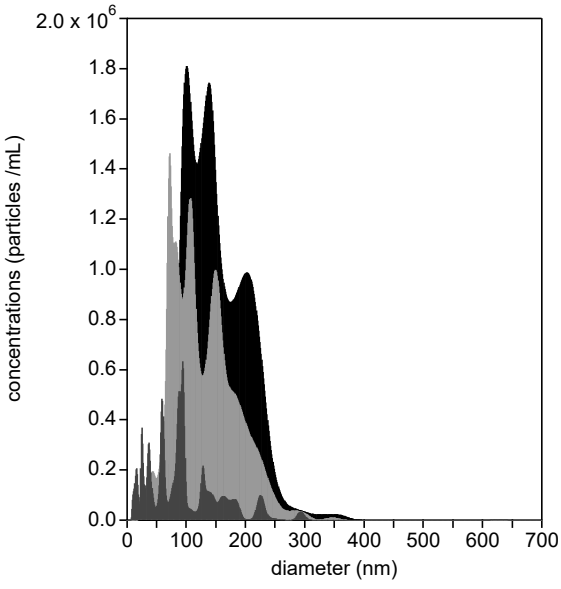


Fig. 1. Nanoparticle tracking analysis of incubated p53-DBD solutions. Black indicates without a reagent, dark gray and light gray indicate moderate and high concentration of a reagent, respectively.

## CO6-20

# High-resolution in vivo imaging of $^{211}$At-labeled radioactive gold nanoparticles

N. Koshikawa[1], Y. Kikuchi[1], R. Tanaka[1], K. Takahashi[2], T. Kadonaga[2], H. Kato[2], K. Kajiyama[2], M. Murakami[2], A. Toyoshima[2], K. Takamiya[3], J. Kataoka[1]

[1] *Graduate School of Advanced Science and Engineering, Waseda University, Tokyo, Japan*
[2] *Institute for Radiation Sciences, the University of Osaka, Osaka, Japan*
[3] *Institute for Integrated Radiation and Nuclear Science, Kyoto University, Kyoto, Japan*

**INTRODUCTION:** Drug delivery systems (DDS) that deliver drugs to tumors have attracted attention to enhance treatment efficacy. Gold nanoparticles (AuNPs) are promising drug carriers, and $^{211}$At-labeled AuNPs have been actively studied because the alpha particles emitted by $^{211}$At provide strong local therapeutic effects[1]. However, the pharmacokinetics of AuNPs remain insufficiently understood. To address this issue, we proposed an "activation imaging" of AuNPs, in which stable $^{197}$Au is irradiated with low-energy neutrons and converted into the radioisotope $^{198}$Au[2]. The [$^{198}$Au]AuNPs can then be visualized using the 412-keV gamma rays emitted by $^{198}$Au.

**EXPERIMENTS:** The AuNP precursor, $HAuCl_4$, was irradiated with neutrons at the Pn-2 beamline of the Kyoto University Research Reactor (KUR). [$^{198}$Au]AuNPs were then synthesized, and $^{211}$At was labeled onto them (Fig. 1(a)). The $^{211}$At-[$^{198}$Au]AuNPs were administered to tumor-bearing mice intratumorally. Imaging was performed using a high-contrast SPECT (HC-SPECT) detector[3] (Fig. 1(b)), which consists of a $Gd_3Al_2Ga_3O_{12}$ (GAGG) scintillator array and tungsten collimator, both with a 1 mm pitch. The HC-SPECT employs novel hourglass-shaped collimator, which allows more gamma rays to reach the scintillator, thereby improving image contrast. After imaging, the mice were dissected and the radioactivity of each organ was measured.

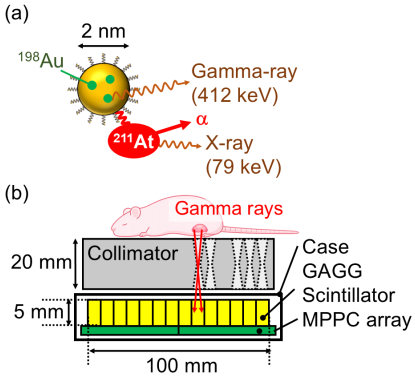


Fig. 1 (a) $^{211}$At-[$^{198}$Au]AuNPs. (b) HC-SPECT.

**RESULTS:** Fig. 2(a) (*left*) and (*right*) show the $^{198}$Au and $^{211}$At images obtained 12 min after administration, respectively. Image of $^{211}$At was obtained by detecting 79-keV X-rays from $^{211}$At. For $^{198}$Au imaging, maximum-likelihood expectation maximization (MLEM) was applied to improve image contrast. Fig. 2(b) and 2(c) show the $^{198}$Au images obtained 3 h and 20 h after administration, respectively. These results indicate that the AuNPs injected into the tumor gradually spread throughout the body. Figure 2(d) shows the radioactivity (%ID/g) of each organ measured 4 days after administration. The tumor showed the highest accumulation, consistent with the imaging results.

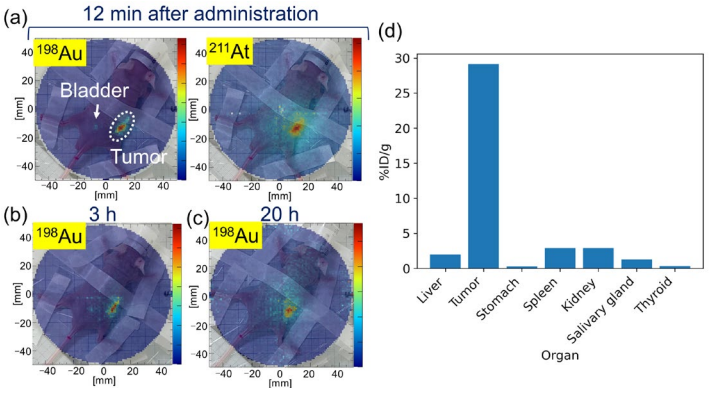


Fig. 2. Images of $^{211}$At-[$^{198}$Au]AuNPs in mice. (a) Distribution of [$^{198}$Au]AuNPs (*left*) and $^{211}$At (*right*) 12 min after injection. Distribution of [$^{198}$Au]AuNPs (b) 3 hours and (c) 20 hours after administration. (d) Radioactivity ($^{198}$Au) of each organ.

**REFERENCES:**

[1] H. Kato *et al.*, J. Nanobiotechnol., **19** (2021) 223.
[2] N. Koshikawa *et al.*, Appl. Phys. Lett., **126** (2025) 103702.
[3] N. Koshikawa *et al.*, J. Instrum., **20** (2025) C07057.

# CO6-21

## Screening of enzymes for Asp isomerization in cells constituting the rat lens

N. Fujii[1], M. Yurugi[2], K. Tanaka[2] and T. Takata[3]

[1] *Radioisotope Research Center, Teikyo University*
[2] *Dept of Chemistry, Graduate School of Science, Kyoto University*
[3] *Institute for Integrated Radiation and Nuclear Science, Kyoto University*

**INTRODUCTION:** Age-related covalent post-translational modifications play a critical role in protein homeostasis. One of the age-related modifications is isomerization of aspartate residues (Asp). If Asp isomerization is regarded as a new quality index for proteins, then suppression of this isomerization can be considered as maintenance of protein quality at the molecular level. Focusing on this concept, our aims to investigate the enzyme protein L-isoaspartyl (D-aspartyl) methyltransferase (PIMT), which suppresses Asp isomerization *in vivo*[1]. PIMT recognizes isomerized Asp residues in proteins and converts them back to a succinimide intermediate, which is subsequently hydrolyzed to restore the normal Asp residue. The distribution of PIMT has been partially characterized and is known to be widespread in tissues such as the brain and muscle. However, intriguingly, PIMT has not been identified in the lens tissue, particularly in the rat lens, where its substrate—isomerized Asp— accumulates in large amounts. The reported absence of PIMT in the lens, despite its expected role as a cellular defense mechanism, appears inconsistent with the maintenance of biological homeostasis. To clarify this contradiction, the present study aims to screen for PIMT in the rat lens.

**EXPERIMENTS:** Rat lenses will be isolated, and PIMT will be screened using RT-PCR and western blotting. Rat kidney and rat lens tissues were homogenized, and total RNA was extracted from each sample using the NucleoSpin RNA Plus kit (Takara). The extracted total RNA was reverse-transcribed using the ReverTra Ace qPCR RT Master Mix (TOYOBO), and the resulting cDNA was analyzed by agarose gel electrophoresis to investigate PIMT gene expression. Both supernatants from homogenates were also subjected to SDS-PAGE. After electrophoresis, proteins were transferred onto a PVDF membrane, and Western blotting was performed using a PCMT1 rabbit polyclonal antibody as the primary antibody and an HRP-conjugated affinipure goat anti-rabbit IgG (H+L) as the secondary antibody.

**RESULTS:** As shown in Fig. 1 (a), the presence of cDNA was confirmed in both the kidney and the lens, suggesting that PIMT is present in both tissues. In contrast, as shown in Fig. 1 (b), Western blotting confirmed PIMT expression in the kidney, whereas its expression in the lens was not detected. These results indicate that, in the lens, PIMT is present at the DNA level but not expressed at the protein level. This discrepancy may reflect species-specific differences between humans and rats, such as lifespan and exposure to external stresses, suggesting the existence of regulatory mechanisms controlling gene expression. Further investigation of these mechanisms will be the subject of future studies.

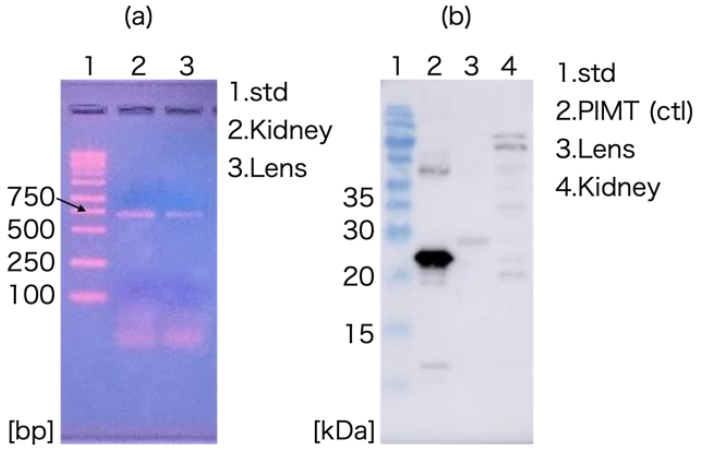


Fig. 1. DNA and Protein expression of PIMT
(a) 3% Agarose gel, (b) Western blotting

**REFERENCES:**

[1] S. Clarke *et al.*, Ageing Res. Rev., **2** (2003) 263-285.

# CO6-22

## Domain-selective Solution Structure Analysis of ER-60 with Segment Deuteration

A. Okuda, M. Shimizu, K. Morishima, R. Inoue, R. Urade and M. Sugiyama

*Institute for Integrated Radiation and Nuclear Science, Kyoto University*

**INTRODUCTION:** ER-60 is an enzyme responsible for oxidative protein folding. ER-60 possesses an **a**-**b**-**b'**-**a'** four-domain structure and regulates substrate folding depending on the redox state of its active site. However, its molecular mechanism remains poorly understood. Because domain configurations dynamically fluctuate in solution, structural analysis at the nanoscale is essential. This study aims to elucidate the domain-level structure and dynamics of ER-60 [1].
In this study, we perform analyses by combining solution scattering methods with molecular dynamics (MD) simulations. Since it is difficult to resolve domain motion using small-angle X-ray scattering (SAXS) alone, we employ domain-selective analysis using small-angle neutron scattering (SANS). Specifically, segmentally deuterated samples are prepared by connecting deuterated and hydrogenated domains via protein ligation [2], enabling selective observation of scattering from specific domains (DS-iCM-SANS) [3].
**EXPERIMENTS:** The 75% deuterated (*d*) and hydrogenated (*h*) domains were expressed in *E. coli* cultured in M9 medium containing 75% deuterium and LB medium without deuterium, respectively [4]. The deuteration level of *d*(**bb'**) domain was evaluated by MALDI-TOF mass spectrometry (MS). The domains (20 μM each) were mixed in buffer containing 200 mM Tris-HCl (pH 7.4) and 150 mM NaCl. The ligation enzyme *Oa*AEP (0.2 μM) was then added, and the protein ligation reaction was performed at 20°C for 64 hours. The reaction products were analyzed by SDS-PAGE. The monodispersity of the samples was evaluated by analytical ultracentrifugation (AUC). SAXS measurements were performed at 25 °C using a NANOPIX (Rigaku, Tokyo, Japan). The sample-to-detector distances were 1330 mm and 300 mm, and the $q$ range was 0.01-0.80 Å $^{-1}$.
**RESULTS:** MALDI-TOF MS spectra showed that *d*(**bb'**) exhibited a distinct mass shift from *h*(**bb'**) (Fig. 1). The deuteration ratio of *d*(**bb'**) was calculated to be 72.5%. This *d*(**bb'**) was used for a ligation reaction to prepare *h*(**a**)-*d*(**bb'**)-*h*(**a'**). The AUC analysis of wild-type and *h*(**a**)-*d*(**bb'**)-*h*(**a'**) ER-60 showed that the samples consisted predominantly of a single species. However, because minor dimeric and trimeric aggregates were present, size-exclusion chromatography-coupled SANS (SEC-SANS) was employed for the SANS measurement to eliminate these aggregates. SEC-SANS experiments have been performed, and data analysis is currently underway.

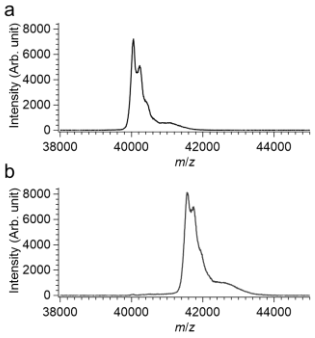


Fig. 1. MALDI-TOF mass spectra of (a) *h*(**bb'**) and (b) *d*(**bb'**). The deuteration ratio of *d*(**bb'**) was 72.5%.

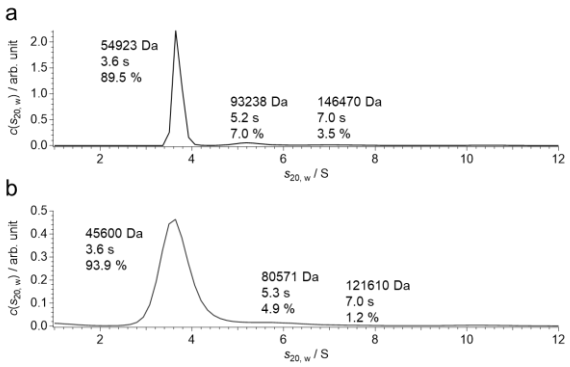


Fig. 2. The AUC profiles of (a) wild-type and (b) *h*(**a**)-*d*(**bb'**)-*h*(**a'**)

**REFERENCES:**

[1] A. Okuda *et al.*, Sci Rep., **11** (2021) 5655.
[2] A. Okuda *et al.*, Angew Chem Int Ed Engl., **62** (2023) e202214412.
[3] M. Sugiyama *et al.*, J. Appl. Cryst, **47** (2014) 430-435.
[4] A. Okuda *et al.*, Biophys Physicobiol., **18** (2021) 16-27.

# CO6-23

# Design, Synthesis, and Evaluation of Hydrophobic Bis(borono) Macrocyclic Polyamines for Boron Neutron Capture Therapy (BNCT)

S. oki[1,2], H. Ueda[3], W. Yoshida[1], M. Suzuki[3], Tanaka, T.[1,4] S Masunaga[3], N. Kondo[3], and Y. akurai[3]

[1]*Faculty of Pharmaceutical Sciences, Tokyo University of Science*
[2]*Research Institute for Science and Technology, Tokyo University of Science*
[3]*Research Reactor Institute, Kyoto University*
[4]*Faculty of Pharmaceutical Sciences, Okayama University*

**INTRODUCTION:** Neutron capture therapy using boron-10 ($^{10}$B) (BNCT) is one of powerful therapies for local tumor control in the treatment of brain tumor, melanoma, and related diseases. We previously designed and synthesized phenylboronic acid-pendant 9-, 12-, and 15-membered macrocyclic amines such as **$^{10}$B-1a~3a** and the corresponding $Zn^{2+}$ complexes **$^{10}$B-1b~3b** (Fig. 1) [1,2], based on high intracellular uptake of cyclen (1,4,7,10-tetraazacyclododecane) derivatives in cancer cells. It was reported that the metal-free **$^{10}$B-1a~3a** are introduced into cancer cells (A549 and HeLa S3 cells) more efficiently than their $Zn^{2+}$ complexes **$^{10}$B-1b~3b** with considerably high cancer/normal cells selectivity. Besides, it was found that 12- and 15-membered derivatives **$^{10}$B-2a~3a** exhibit a higher BNCT effect than **$^{10}$B-1a**, possibly because **$^{10}$B-2a~3a** form the corresponding $Zn^{2+}$ complexes **$^{10}$B-2b** & **3b**, which strongly interact with DNA in living cells [3], resulting in the efficient breakdown of DNA upon the neutron irradiation. Dimeric macrocyclic polyamines having one phenylboronic acid unit such as **4**~**9** and their corresponding $Zn^{2+}$ complexes (Fig. 1), because it was well established that polymeric $Zn^{2+}$ complexes would form more stable complexes with DNA double strand than monomeric $Zn^{2+}$ complexes [4]. However, the intracellular uptake of **4**~**9** and their $Zn^{2+}$ complexes were lower than monomeric compounds **1**~**3**, possibly due to their lower hydrophobicity than that of **1**~**3.**

These data prompted us to design and synthesize monomeric polyamines equipped with two boronic ester units **10a**~**15a** and their corresponding $Zn^{2+}$ complexes **10b**~**15b** shown in Fig. 1for higher intracellular uptake and BNCT effect.

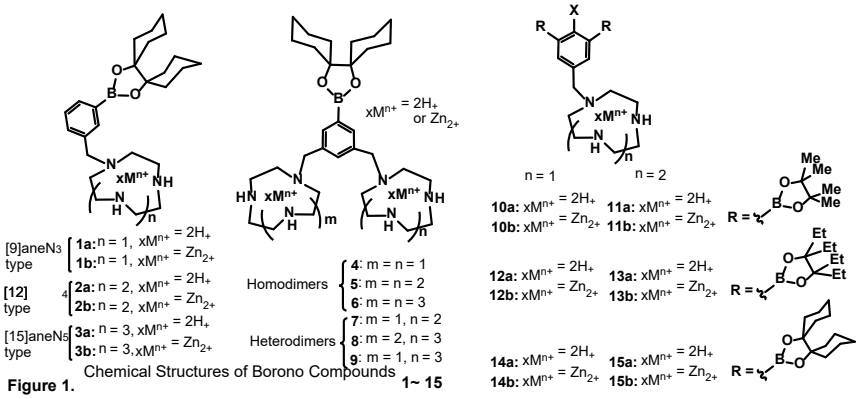


**Figure 1.** Chemical Structures of Borono Compounds **1~ 15**

## EXPERIMENT AND RESULTS:

In 2025, **10a**~**15a** and their corresponding $Zn^{2+}$ complexes **10b**~**15b** (Fig. 1) were synthesized. The evaluation of intracellular uptake and BNCT effect of **10a**~**15a** and **10b**~**15b** has suggested that more hydrophobic **14a** has highest intracellular uptake and BNCT effect among these compounds [5].

## REFERENCES:

[1] H. Ueda, et al. *J. Med. Chem.* **64** (2021) 8523-8544.
[2] S. Aoki, et al. In "*Characteristics and Applications of Boron*" 2022, pp 83-105, Charchawal Wongchoosuk, Ed., IntechOpen, Croatia.
[3] S. Aoki, E. Kimura, *Chem. Rev.* **104** (2004) 769-788.
[4] H. Ueda, et. al. *Eur. J. Inorg. Chem.* **2022** (2022) e202100949 (24 pages).
[5] W. Yoshida, et al. Manuscript in preparation.

CO6-24

# Characterization of DNA Damage and Mutagenesis Induced by Reactor-Generated Neutron Beams

H. Terato[1], T. Hanafusa[2], M. Isobe[1], Y. Sakurai[3], and T. Saito[3]

[1]*Advanced Science Research Center, Okayama University*
[2]*Neutron Therapy Research Center, Okayama University*
[3]*Institute for Integrated Radiation and Nuclear Science, Kyoto University*

**INTRODUCTION:** Biological effects of radiation are primarily mediated by genomic DNA damage. Consequently, detailed analysis of such damage is fundamental to elucidating the molecular mechanisms underlying these effects. Our previous studies have demonstrated that high linear energy transfer (LET) radiation, such as heavy-ion beams, yields DNA damage profiles distinct from those induced by low-LET radiation, like γ-rays [1, 2]. As another form of high-LET radiation, neutron beams are expected to exhibit specific patterns of DNA damage. Our earlier collaborative research indicated that neutron radiation possesses a higher relative biological effectiveness (RBE) for DNA damage induction and cytotoxicity compared to γ-rays. The biological consequences of DNA damage generally follow two pathways: (i) the direct inhibition of DNA replication leading to cell death, and (ii) the induction of mutations that impair cellular functions. Given that heavy-ion radiation produces a mutation spectrum distinct from that of γ-rays [3], it is hypothesized that neutron radiation also induces characteristic mutations. In this study, we aimed to characterize the mutation spectrum induced by neutron irradiation using a plasmid-based assay.

**EXPERIMENTS:** pUC19 plasmid DNA was dissolved in TE buffer (10 mM Tris-HCl, pH 7.5; 1 mM EDTA). Samples were prepared with or without 10% (w/v) BSH ($^{10}$B-sodium mercaptododecaborate), a boron neutron capture therapy (BNCT) agent. Neutron irradiation was performed at the Kyoto University Reactor (KUR). The total physical dose, including both neutrons and concomitant γ-rays, was set up to 5 Gy. Following irradiation, the DNA was transformed into competent Escherichia coli cells to assess mutagenesis. Mutations within the lacZα gene were screened via the α-complementation assay (blue/white screening), and the mutation spectrum was analyzed by DNA sequencing of the resulting white colonies, according to previously established protocols [3].

**RESULTS:** Initial screening via the α-complementation assay identified a small number of white colonies (data not shown). However, subsequent DNA sequencing failed to confirm any specific mutations within the lacZ region of these colonies. This result is likely attributable to the limited radiation dose applied in this study. Although neutron radiation exhibits high RBE, the maximum dose was restricted to 5 Gy due to constraints on reactor machine time, which may have been insufficient to induce mutation frequencies above the detection threshold. Notably, even in samples containing BSH—where the $^{10}$B (n, alpha) $^{7}$Li reaction was expected to enhance local energy deposition—no confirmed mutations were observed. These findings suggest that within the 0–5 Gy dose range, neutron-induced biological effects might be predominantly mediated by the direct inhibition of DNA replication rather than by the accumulation of point mutations or small deletions detectable by this assay. Further studies utilizing higher doses or more sensitive detection systems are required to further characterize the mutagenic potential of neutron beams.

**REFERENCES:**

[1] H. Terato *et al*., J. Radiat. Res., **49** (2008) 133-146.
[2] Y. Tokuyama *et al*., J. Radiat. Res., **56** (2015) 446-455.
[3] Y. Tokuyama *et al*., J. Radiat. Res., **65** (2024) 491-499.

# CO6-25

## Study of Imaging System for Ultra-High Dose Rate Irradiation Field

N. Matsubayashi [1], T. Takata [1], K. Fuchigami [2], N. Abe [1], T. Takahashi [1], and H. Tanaka[1]

[1] *Institute for Integrated Radiation and Nuclear Science, Kyoto University*
[2] *Graduate School of Engineering, Kyoto University*

**INTRODUCTION:** In ultra-high dose rate (UHDR) irradiation field, the FLASH effect has been confirmed, which minimizes damage to normal tissue while maintaining unaltered tumor control [1, 2]. The precise mechanism underlying the FLASH effect is unclear. To verify this, it is important to establish a method for evaluating the irradiation field. In this study, we developed the system that measures the two-dimensional distribution of the UHDR irradiation field in real-time by visible light emitted from an acrylic plate using a CMOS camera.

**EXPERIMENTS:** The schematic layout of the imaging system is shown in Fig. 1. Since luminescence can be observed even in air by electron, the acrylic plate was made 4 cm thick to stop the electron, and blocked light from all directions except that toward the camera. The irradiation tests were performed at the electron linear accelerator in KURNS (KURNS-LINAC). The electron beam energy was set to 8 MeV, and the pulse width was set to 5 μs. Measurements were taken while varying the distance between the beam port and the acrylic plate from 0 to 600 mm at 100 mm intervals. The distributions were normalized using the results from Radio-chromic films, a common measurement method for UHDR irradiation field, irradiated under the same conditions.

**RESULTS:** Fig. 2 shows the lateral distribution as a function of distance from the beam port. It was found that the normalized factors are varied by 30% depending on the distance, but the peak intensities roughly corresponded to those of the films. However, the distribution was broader than the films; this is due to the scattering of electrons in the 4 cm thick acrylic. In conclusion, we investigated a method for evaluation of two-dimensional dose distributions using CMOS camera in UHDR irradiation field. Although we were unable to obtain distributions equivalent to the conventional methods, we were able to get the peak position in real-time, suggesting that this method could be used for monitoring the peak positions.

**REFERENCES:**

[1] V. Favaudon et al., Sci. Transl. Med. 6, 245(2014)
[2] J. Bourhis et al., Radi. Onco. 139, p11-17(2019)

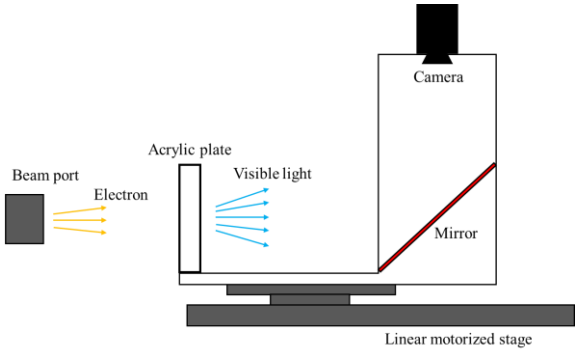


Fig. 1. Schematic layout of imaging system using acrylic plate and CMOS camera.

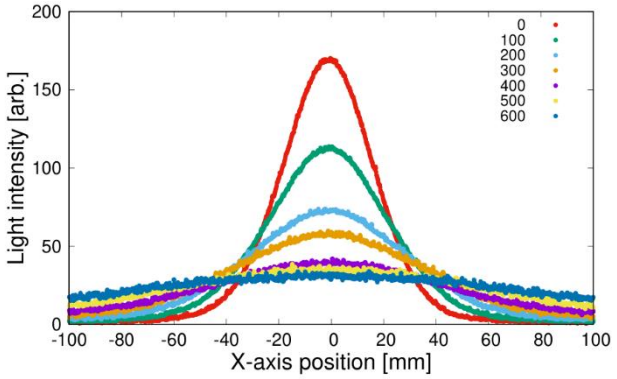


Fig. 2. Lateral distributions measured by CMOS camera while varying the distance from beam port (0~600 mm).

# CO6-26

# $^{10}$B-enriched nitroimidazole derivative with high water solubility as a functional drug for hypoxia-targeting boron-neutron capture therapy

K. Tanabe,[1] T. Nishihara,[1] H. Bamba[1] and M. Suzuki[2]

[1]*Department of Chemistry and Biological Science, College of Science and Engineering, Aoyama Gakuin University*
[2]*Institute for Integrated Radiation and Nuclear Science, Kyoto University*

## INTRODUCTION:

Boron neutron capture therapy (BNCT) is a promising radiotherapy based on the nuclear reaction between boron-10 ($^{10}$B) and thermal neutrons. The therapeutic efficacy of BNCT depends on the development of boron-containing agents that selectively accumulate in cancer cells. In particular, the development of BNCT agents effective against hypoxic cells is highly desirable, since tumor hypoxia is closely associated with resistance to conventional therapies.

In our previous study, we developed BPA-NI, a nitroimidazole (NI)-containing derivative of $^{10}$B-enriched *p*-boronophenylalanine (BPA), as a hypoxia-targeting BNCT agent, and confirmed its selective accumulation in hypoxic cells together with its cytotoxic effect upon thermal neutron irradiation.[1] On the other hand, improvement of its water solubility remained an important challenge. To address this issue, in the present study we designed a new BNCT agent using a nucleobase capable of forming a complex with BPA, with the aim of improving the aqueous solubility of the BPA-NI-based system while maintaining hypoxia-targeting ability. Since nitroimidazoles are well known as exogenous hypoxia markers owing to their characteristic bioreductive behavior in hypoxic cells, an NI-containing BPA–nucleobase complex (BPA-NI-U) was prepared and evaluated. Herein, we describe its preparation, selective accumulation in hypoxic cells, and cytotoxic effect under thermal neutron irradiation.

## EXPERIMENTS:

The BPA-NI-U (0 or 500 μM) was administered to the SAS cells and then the cells were incubated for 20 h. After incubation and wash, the cells were irradiated (neutron, 1 MW) for 45 min at KUR. After incubation, WST 8 was added to the cells, and the cell viability assay was performed using Microplate Reader.

## RESULTS:

SAS cells were selected as the target cell line because of their suitability for BNCT studies, and the cytotoxic effect of BPA-NI-U under thermal neutron irradiation was evaluated. After incubation with BPA-NI-U for 20 h under either hypoxic or aerobic conditions, the cells were exposed to neutron irradiation. BPA-NI-U showed little cytotoxicity in aerobic SAS cells, whereas markedly enhanced cytotoxicity was observed in hypoxic SAS cells. By contrast, BPA alone induced cytotoxicity in both aerobic and hypoxic cells without hypoxia selectivity. Taken together, these results indicate that BPA-NI-U preferentially accumulated in hypoxic cells, thereby exerting selective cytotoxic effects upon thermal neutron irradiation.

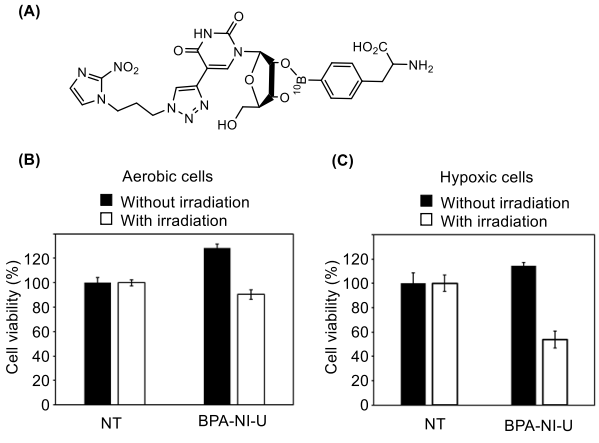


Fig. 1. (A) Chemical structure of BPA-NI-U. ((B) Cytotoxicity of BPA-NI-U against SAS cells upon thermal neutron irradiation under aerobic (B) or hypoxic conditions (C).

## REFERENCES:

[1] K. Tanabe *et al.*, Results Chem., **15** (2025) 102245.

## CO6-27

# Tritium Labeling of Eggshell Membrane, a Natural Composite Biomaterial, via the $^{6}Li(n,\alpha)^{3}H$ Reaction at KUR Pn-2 for Biodistribution Studies

M Shimizu[1], E. Ohto-Fujita[1], N. Nogawa[2], H. Yoshinaga[3], K. Takamiya[3], A. Enomoto[4], T. Yamashita[5], Y. Asano[6], Y. Hasebe[7], and Y. Atomi[1]

[1]*Teikyo University, Advanced Comprehensive Research Organization, Division of Open Innovation*
[2]*Isotope Science Center, The University of Tokyo*
[3]*Institute for Integrated Radiation and Nuclear Science, Kyoto University*
[4]*Isotope Facility, Graduate School of Medicine, The University of Tokyo*
[5]*Department of dermatology, Graduate School of Medicine, The University of Tokyo*
[6]*Department of Dermatology, Tohoku University Graduate School of Medicine*
[7]*Almado, Inc.*

**INTRODUCTION:** Inflammatory bowel disease (IBD) causes intestinal fibrosis and stricture through chronic inflammation, severely impairing patients' quality of life. Intestinal fibrosis is characterized by excessive ECM accumulation and tissue stiffening, with few fundamental therapies available once it progresses. Notably, ECM also governs stem cell niches and epithelial regeneration, suggesting that fibrosis may be controllable as a reversible remodeling process. Eggshell membrane (ESM) is a traditional wound-healing material composed mainly of fibrous proteins. Using $^{3}H$-labeled ESM prepared via the $^{6}Li(n,\alpha)^{3}H$ reaction—a labeling method originally developed at JRR-4 [1] and applied in the present study at KUR—we have investigated its in vivo behavior and biological functions. In a previous study, we reported that oral ESM alleviates lung fibrosis demonstrated that ESM and its major component, lysozyme (LYZ), act as anti-fibrotic agents against pulmonary fibrosis via decorin induction and TGF-β suppression [2]. However, the in vivo kinetics of ESM and its mechanisms of action on the intestinal environment remain largely unclear.
In this study, we quantified the biodistribution of $^{3}H$-labeled ESM after oral administration and evaluated its effects on intestinal fibrosis and the gut environment, aiming to establish a foundation for novel preventive and therapeutic strategies [3].
**EXPERIMENTS:** ESM powder was sealed in a quartz tube together with lithium carbonate, and $^{3}H$ was introduced by neutron irradiation via the $^{6}Li(n,\alpha)^{3}H$ reaction at KUR Pn-2. The $^{3}H$-labeled ESM was mixed with jelly and administered orally to mice, and blood, major organs, and feces were collected at multiple time points ranging from 0.5 to 72 hours after administration. The amount of $^{3}H$ was measured by liquid scintillation counting, and the tissue distribution was calculated. Statistical analyses were performed using ANOVA followed by appropriate multiple comparison tests.
**RESULTS:** Following oral administration of $^{3}H$-labeled ESM, the radioactivity in blood reached its peak at 5 hours post-administration and gradually declined thereafter. In the gastrointestinal tract, an early peak was observed in the duodenum and small intestine at 2 hours post-administration, followed by widespread distribution to the large intestine, liver, kidney, lung, and skin. The radioactivity in rectal feces reflected the excretion of undigested components and indicated the presence of ESM-derived components retained within the intestinal lumen; however, these components were excreted relatively rapidly.
**Conclusion:** The KUR Pn-2 irradiation facility proved highly suitable for tritium labeling of protein samples, as it maintains low sample temperatures during neutron irradiation and thereby preserves the integrity of biological materials. However, given that KUR ceased operation in April 2026, we strongly hope that comparable irradiation capabilities will be implemented in the newly planned successor reactor to enable the continuation of such studies.
**********

**REFERENCES:** [1] E. Ohto-Fujita et al., J. Fiber Sci. Technol., 77 (2021) 182-187. doi.org/10.2115/fiberst.2021-0018. [2] E. Ohto-Fujita et al., Biochem. Biophys. Rep., 39 (2024) 101806. doi:10.1016/j.bbrep.2024.101806. [3] M. Shimizu et al., Int. J. Mol. Sci., 26 (2025) 9102. doi: 10.3390/ijms26189102.

# CO6-28

# Design, Synthesis, and Evaluation of Multiborono Polyamines for Boron Neutron Capture Therapy (BNCT)

S. Aoki[1,2], H. Ueda[3], W. Yoshida[1], M. Suzuki[3], T. Tanaka[1,4], S Masunaga[3], N. Kondo[3], and Y. Sakurai[3]

[1]*Faculty of Pharmaceutical Sciences, Tokyo University of Science*
[2]*Research Institute for Science and Technology, Tokyo University of Science*
[3]*Research Reactor Institute, Kyoto University*
[4]*Faculty of Pharmaceutical Sciences, Okayama University*

**INTRODUCTION:** Neutron capture therapy using boron-10 ($^{10}$B) (BNCT) is one of powerful therapies for local tumor control in the treatment of brain tumor, melanoma, and related diseases. We previously designed and synthesized phenylboronic acid-pendant 9-, 12-, and 15-membered macrocyclic amines such as **$^{10}$B-1a~3a** and the corresponding $Zn^{2+}$ complexes **$^{10}$B-1b~3b** (Fig. 1) [1,2], based on high intracellular uptake of cyclen (1,4,7,10-tetraazacyclododecane) derivatives in cancer cells (A549 cells). It was reported that the metal-free **$^{10}$B-1a~3a** are introduced into cancer cells (A549 and HeLa S3 cells) more efficiently than their $Zn^{2+}$ complexes **$^{10}$B-1b~3b** with considerably high cancer/normal cells selectivity. Besides, it was found that 12- and 15-membered derivatives **$^{10}$B-2a~3a** exhibit a higher BNCT effect than **$^{10}$B-1a**, possibly because **$^{10}$B-2a~3a** form the corresponding $Zn^{2+}$ complexes **$^{10}$B-2b** & **3b**, which strongly interact with DNA in living cells [3], resulting in the efficient breakdown of DNA upon the neutron irradiation.

Next, we conducted the design and synthesis of monomeric polyamines equipped with two boronic ester units **4a**~**9a** and their corresponding $Zn^{2+}$ complexes **4b**~**9b** (Fig. 1) for higher intracellular uptake of $^{10}$B atoms and more potent BNCT effect.

**EXPERIMENTS AND RESULTS:**

The synthesis of **4a**~**9a** and their corresponding $Zn^{2+}$ complexes **4b**~**9b** was carried out and their intracellular uptake and BNCT effect were found to be highest among these compounds [4]. In addition, the effect of addition of $Zn^{2+}$ from outside on BNCT effect of these $^{10}$B carriers was evaluated, because it was expected that the $Zn^{2+}$ complexes **4b**~**9b** were supposed to recognize the deprotonate thymidine in DNA in order to place $^{10}$B units at the close position to DNA for more efficient BNCT effect. The results of BNCT experiments have suggested that the effect of $Zn^{2+}$-pyrithione complex on BNCT effect of **4a**~**9a** is not so significant, suggesting that the concentrations of $Zn^{2+}$ in A549 cells are high enough to form their $Zn^{2+}$ complexes in cells.

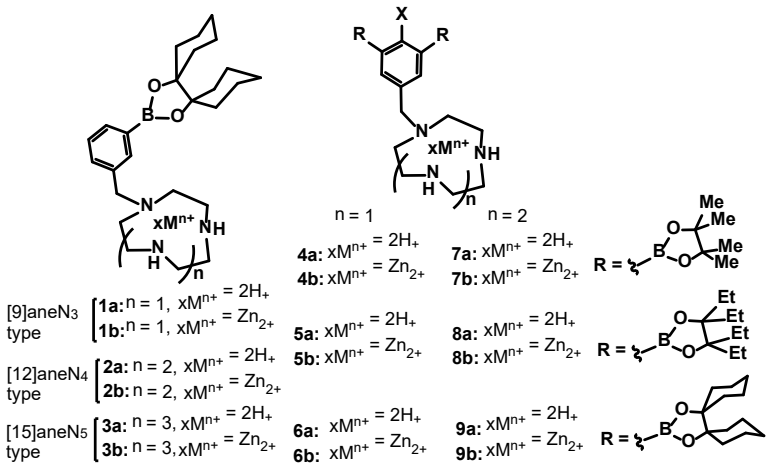


**Figure 1.** Chemical Structures of Borono Compounds **1 ~ 9**

**REFERENCES:**

[1] H. Ueda, et al. *J. Med. Chem.* **64** (2021) 8523-8544.
[2] S. Aoki, et al. In "*Characteristics and Applications of Boron*" 2022, pp 83-105, Charchawal Wongchoosuk, Ed., IntechOpen, Croatia.
[3] S. Aoki, E. Kimura, *Chem. Rev.* **104** (2004) 769-788.
[4] W. Yoshida, et al. Manuscript in preparation.